SPECIAL
RELAMPAGO-CACTI
COLLECTION

A Synoptic Evolution Comparison of the Smallest and Largest MCSs in Subtropical South America between Spring and Summer

JEREMIAH O. PIERSANTE,[a] KRISTEN L. RASMUSSEN,[a] RUSS S. SCHUMACHER,[a] ANGELA K. ROWE,[b] AND LYNN A. MCMURDIE[c]

[a] *Department of Atmospheric Science, Colorado State University, Fort Collins, Colorado*
[b] *Department of Atmospheric Science, University of Wisconsin–Madison, Madison, Wisconsin*
[c] *Department of Atmospheric Sciences, University of Washington, Seattle, Washington*

(Manuscript received 25 June 2020, in final form 25 March 2021)

ABSTRACT: Subtropical South America (SSA) east of the Andes Mountains is a global hotspot for mesoscale convective systems (MCSs). Wide convective cores (WCCs) are typically embedded within mature MCSs, contribute over 40% of SSA's warm-season rainfall, and are often associated with severe weather. Prior analysis of Tropical Rainfall Measuring Mission (TRMM) Precipitation Radar (PR) data identified WCCs in SSA and associated synoptic conditions during austral summer. As WCCs also occur during the austral spring, this study uses the 16-yr TRMM PR and ERA5 datasets to compare anomalies in environmental conditions between austral spring (SON) and summer (DJF) for the largest and smallest WCCs in SSA. During both seasons, large WCCs are associated with an anomalous midlevel trough that slowly crosses the Andes Mountains and a northerly South American low-level jet (SALLJ) over SSA, though the SON trough and SALLJ anomalies are stronger and located farther northeastward than in DJF. A synoptic pattern evolution resembling large WCC environments is illustrated through a multiday case during the RELAMPAGO field campaign (10–13 November 2018). Unique high-temporal-resolution soundings showed strong midlevel vertical wind shear associated with this event, induced by the juxtaposition of the northerly SALLJ and southerly near-surface flow. It is hypothesized that the Andes help create a quasi-stationary trough–ridge pattern such that favorable synoptic conditions for deep convection persist for multiple days. For the smallest WCCs, anomalously weaker synoptic-scale forcing was present compared to the largest events, especially for DJF, pointing to future work exploring MCS formation under weaker synoptic conditions.

KEYWORDS: South America; Synoptic-scale processes; Mesoscale systems; Radars/Radar observations; Radiosonde/rawinsonde observations; Mountain meteorology

1. Introduction

Thunderstorms maximize in frequency and intensity near large mountain ranges (Zipser et al. 2006); however, ground-based observations are historically sparse in some of these locations around the world. Fortunately, the Tropical Rainfall Measuring Mission (TRMM) Precipitation Radar (PR) has provided a robust dataset of subtropical storm characteristics. Resulting studies using TRMM PR have shown observational evidence that convective echoes east of the Andes Mountains in subtropical South America (SSA) are deeper and more frequent than those east of the Rocky Mountains in North America (Zipser et al. 2006; Houze et al. 2015). Specifically, the cloud shields associated with SSA mesoscale convective systems (MCSs) are approximately 60% larger than those occurring in the continental United States (CONUS; Velasco and Fritsch 1987) and their precipitation areas are larger and longer lived (Durkee et al. 2009; Durkee and Mote 2010), contributing up to ~95% of warm-season rainfall in SSA (Nesbitt et al. 2006; Rasmussen et al. 2016). MCSs are also responsible for the regional maximum in high impact weather such as significant hail (≥2.5-cm diameter), flooding, damaging straight-line winds, and tornadoes that are detrimental to society and the economy of the La Plata basin where agriculture thrives (Rasmussen and Houze 2011; Matsudo and Salio 2011; Cecil and Blankenship 2012; Rasmussen et al. 2014; Bruick et al. 2019).

A typical pattern for the initiation of deep convection in SSA includes an enhanced South American low-level jet (SALLJ) relative to warm-season climatology that advects

Supplemental information related to this paper is available at the Journals Online website: https://doi.org/10.1175/MWR-D-20-0208.s1.

Piersante's current affiliation: Department of Atmospheric and Environmental Sciences, University at Albany, State University of New York, Albany, New York.

Corresponding author: Jeremiah Otero Piersante, jpiersante@albany.edu

DOI: 10.1175/MWR-D-20-0208.1

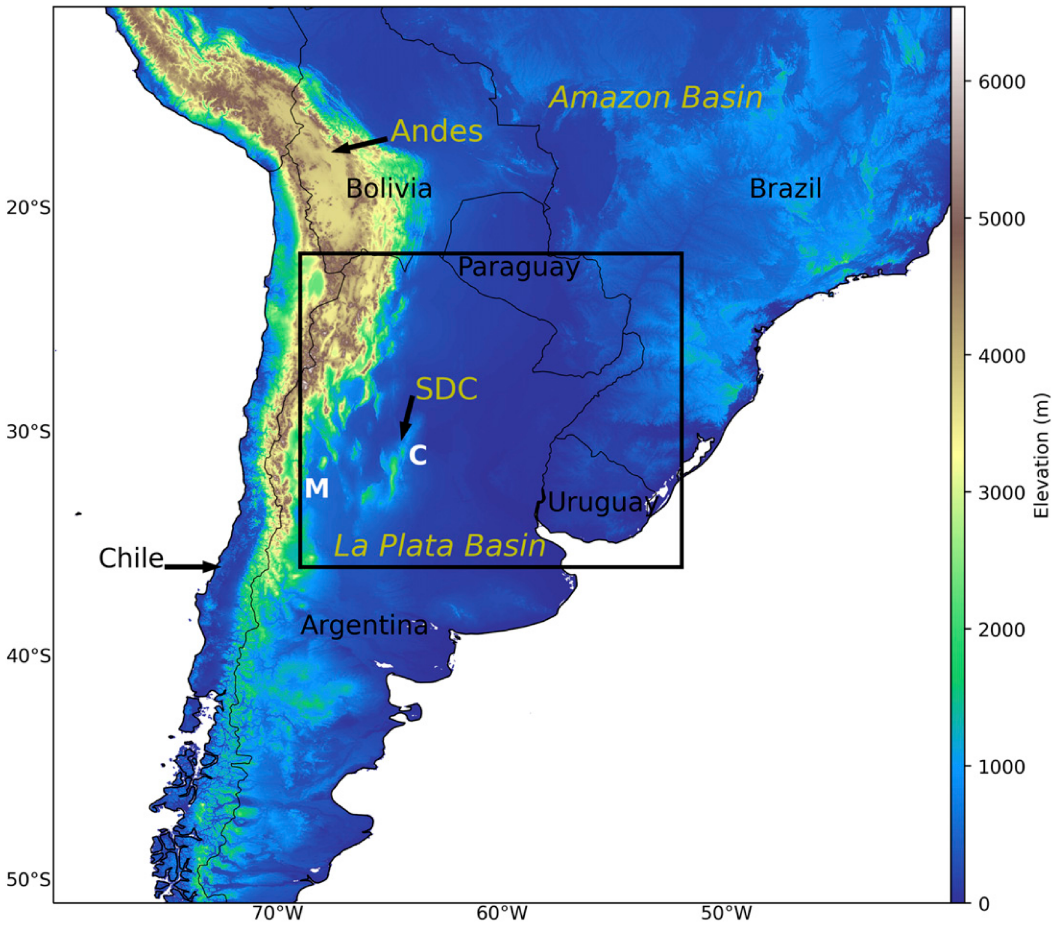

FIG. 1. WCC domain used in this study (black box). This region in subtropical South America, generally referred to as the La Plata basin, includes a portion of the Andes Mountains, the Sierras de Córdoba (SDC) mountain range, and the cities of Mendoza (M) and Córdoba (C) in Argentina. Color shading represents terrain height. Neighboring nations are also labeled.

warm and moist air southward along the Andes Mountains from the Amazon basin into the La Plata basin of northern Argentina (Vera et al. 2006; Insel et al. 2010; Montini et al. 2019; regions shown in Fig. 1). Simultaneously, a deep midlevel trough approaches the Andes from the west, inducing dry mid- to upper-level subsidence flow, which creates a strong capping inversion over the moist air mass east of the Andes. This inversion is sometimes overcome via terrain-induced lift by the Andes foothills and the Sierras de Córdoba (SDC), a secondary mountain range west of the La Plata basin (Fig. 1), in addition to large-scale rising motion, resulting in vigorous deep convection (Romatschke and Houze 2010; Rasmussen and Houze 2011, 2016). These unique topographic features of western Argentina (e.g., Andes foothills, SDC) often act as a platform for ''back-building'' in which deep convection continuously initiates along and remains tied to the mountainous terrain (Rasmussen and Houze 2011; Rasmussen et al. 2014). Typically in SSA, extremely deep convective echoes form during the evening along the terrain and grow upscale into extremely wide cores at night as they expand eastward; this transition from discrete storms into MCSs, commonly referred to as upscale growth, on average occurs within the first ~3 h following convection initiation in SSA, which is relatively fast compared to the CONUS (Mulholland et al. 2018). Furthermore, the increased height of the Andes blocks more midlevel flow, causing enhanced convective available potential energy (CAPE) and convective inhibition (CIN) to develop downstream relative to shorter mountain ranges, which in turn leads to more vigorous deep convection (Rasmussen and Houze 2016). These mechanisms of deep convection initiation in SSA are summarized in a conceptual model by Rasmussen and Houze (2016). Ground-based storm classification via a C-band radar in Córdoba, Argentina (hereafter, Córdoba city), shows similar results to TRMM, such as the proximity of storm initiation near the SDC (Mulholland et al. 2018).

MCS events in SSA can span multiple days, with diurnal resurgences of upscale growth and upstream propagation events (Anabor et al. 2008). Similar long-lived events occur in the CONUS, though less frequently (Augustine and Howard 1988), and it has been shown that the increased longevity of CONUS MCSs is a result of quasi-stationary synoptic waves in addition to various mesoscale phenomena such as vertical wind

shear, convective feedbacks, and cold pool interactions (Stensrud and Fritsch 1993; Stensrud 1996; Laing and Fritsch 2000; Coniglio et al. 2010; Trier et al. 2011; Peters and Schumacher 2015; Yang et al. 2017; Chasteen et al. 2019). Likewise, Rasmussen and Houze (2016) suggest that long MCS lifetimes in SSA are regulated by the slow-moving nature of midlevel troughs approaching the Andes from the west; however, their investigation was limited to the austral summer despite a comparable severe weather and MCS frequency in the La Plata basin during the spring (Rasmussen et al. 2014, 2016). There are likely notable differences in austral spring versus summer MCSs in SSA considering boreal summer MCSs in the CONUS Great Plains tend to be farther poleward and have weaker synoptic and thermodynamic perturbations than spring cases (Song et al. 2019). Thus, a complete understanding of MCS ingredients in SSA requires investigation at synoptic and mesoscales over multiple seasons.

To investigate large-scale differences between MCSs across seasons, this study analyzes the anomalous synoptic environments associated with organized deep convection in both austral spring and summer in SSA. Based on previous studies in the CONUS (Feng et al. 2019; Song et al. 2019), it is hypothesized that spring MCSs are associated with greater anomalous synoptic forcing. Because of this potential shift in synoptic forcing magnitude, we determine whether there is a relationship between anomalous synoptic forcing and MCS area. While area is not a precise method to identify severe weather and hydrologic storm impacts, it allows us to test a hypothesis that larger storms are associated with stronger and more quasi-stationary synoptic forcing. These results are exemplified through a multiday MCS event that occurred during the 2018 Remote sensing of Electrification, Lightning, And Mesoscale/microscale Processes with Adaptive Ground Observations (RELAMPAGO; Nesbitt et al. 2021) field campaign. Long-lived, large MCS events that feature backbuilding deep convection, serial upstream propagation, and severe weather in the form of hail, tornadoes, damaging straight-line winds, and floods like the one discussed herein, are relatively common in SSA; what is uncommon, however, is a high-resolution fixed and mobile sounding dataset in addition to *GOES-16* data that captured this MCS event. These unique data are used to relate the large-scale conditions to mesoscale phenomena contributing to upscale growth, such as vertical wind shear and unique topography. An analysis of this type has yet to take place in SSA because of the sparsity of the data prior to RELAMPAGO. This work not only improves the understanding of the synoptic environments that lead to large and long-lasting MCSs in SSA, but also can be applied to other regions around the world that feature widespread or discrete orographic deep convection.

2. Methodology

Due to the historic lack of a ground-based radar network in SSA, this study uses 16 years (1998–2013) of V7 TRMM PR data (Iguchi et al. 2000, 2009) to identify storms with extreme characteristics during the austral spring [September–November (SON)] and summer [December–February (DJF)]. This satellite-borne precipitation radar provided three-dimensional volume scans of reflectivity with 4–5-km horizontal and 250-m vertical resolution between 37.5°N and 37.5°S during 1997–2014 (Kummerow et al. 1998). We limit our domain to 22°–36°S, 52°–69°W (black box in Fig. 1) to capture the Andes foothills and the La Plata basin region (the plains east of the Andes foothills in Argentina shown in Fig. 1). Our study domain also includes the RELAMPAGO study region, which was centered near the SDC, a smaller, secondary mountain range east of the Andes Mountains (Fig. 1).

TRMM PR data are used to identify convective echoes of extreme horizontal or vertical dimension embedded within MCSs. In addition to substantially contributing to the hydrologic cycle (Rasmussen et al. 2016), radar echo structures imply stages in the MCS life cycle (Houze 2004). Particularly, South American convective echoes with 40-dBZ heights $\geq$ 10 km (deep convective cores; DCCs) indicate young, vigorous convection while those with 40-dBZ areas $\geq 1000\,\text{km}^2$ when projected onto a horizontal plane (wide convective cores; WCCs) represent a later life cycle stage featuring more organized convection that is often associated with long-lived MCSs. As the convective regions of the MCS lose their buoyancy, they tend to develop broad stratiform regions beyond the mature phase (Romatschke and Houze 2010; Rasmussen and Houze 2011, 2016; Rasmussen et al. 2016). This convection life cycle was examined for a case in SSA using available satellite observations and a WRF model simulation that confirmed this life cycle evolution (Rasmussen and Houze 2016), which aligns well with that of other global convective hotspots featuring frequent upscale growth into MCSs over both land and ocean regions (Houze 2004; Zuluaga and Houze 2013; Houze et al. 2015). WCCs are primarily responsible for the regional maximum in high impact weather as they are much more numerous than DCCs in the La Plata basin (see Fig. 5 of Rasmussen and Houze 2011), and they maximize in size, intensity, and frequency in the region (Romatschke and Houze 2010; Rasmussen and Houze 2011). Thus, the identification of WCC environments is the focus of the current study.

To test the hypothesis that larger and thus more impactful WCCs are maintained by a more amplified and quasi-stationary trough–ridge pattern and SALLJ, warm-season WCCs (SON–DJF) during 1998–2013 are divided into two categories: 1) large WCCs, which are those $\geq$ 90th-percentile area ($4880\,\text{km}^2$) and 2) small WCCs, which are $\leq$ 10th-percentile area ($1093\,\text{km}^2$). DJF featured 135 more WCCs of any size than SON, but SON WCCs were on average $64\,\text{km}^2$ larger (Table 1). While the large WCC count was similar between seasons, both the number of small WCCs and unique days on which they occurred was greater in DJF (Table 1). There were some days in which both small and large WCCs were identified by TRMM; these were counted as large WCC days and excluded from small WCC days in an effort to distinguish the synoptic forcing between the two. Last, WCCs that also met the criteria for DCCs were included in this analysis.

Following the methodology used in Rasmussen and Houze (2016), composites of meteorological variables from ERA5 (Copernicus Climate Change Service 2017) illustrate the synoptic environment evolution from 3 days before to 2 days after the detection of a large or small WCC by TRMM. ERA5 has hourly temporal resolution, 1/4° horizontal resolution, and

TABLE 1. WCC count and size during September–November (SON) and December–February (DJF) of 1998–2013 as identified by TRMM PR. Mean area and standard deviation are shown for all WCCs, regardless of size. The number of large (≥90th percentile; 4880 km^2) and small (≤10th percentile; 1093 km^2) WCCs, in addition to the number of days of such occurrences, is also presented. Small WCC days do not include days that also featured large WCCs.

	No. of all WCCs	Area mean (km^2)	Area std dev (km^2)	No. of large WCCs	No. of large WCC days	No. of small WCCs	No. of small WCC days
SON	1909	2626	2479	195	146	185	112
DJF	2044	2562	2475	201	154	211	147
SONDJF	3953	2576	2477	396	300	396	259

137 vertical levels on its native grid, which is a significant upgrade from the NCEP–NCAR reanalysis (Kalnay et al. 1996) used in Rasmussen and Houze (2016). Composites were calculated by averaging hourly conditions on days when a large or small WCC was identified in the study domain by TRMM. Composite anomalies were then calculated by subtracting the climatological long-term average (1979–2018) of the corresponding season from the composite field. This format is used to present the synoptic forcing differences between large and small WCCs in SON and DJF.

These seasonal composite results are compared to a widespread, long-lived MCS event that occurred during RELAMPAGO between 10 and 13 November 2018. Here, ERA5 composite anomalies of meteorological variables were calculated with respect to the November climatological average. We also combine analyses from high-temporal-resolution soundings and *GOES-16* IR brightness temperature images available from RELAMPAGO within the context of ERA5 to investigate synoptic and mesoscale mechanisms supporting this event. Low- to midlevel vertical wind shear is graphically visualized from atmospheric soundings, where CAPE and CIN are calculated via MetPy (May et al. 2020).

3. Seasonal variation of synoptic support of WCCs

Previous studies focused on anomalous synoptic-scale support for MCSs during summertime only (Romatschke and Houze 2010; Rasmussen and Houze 2016). Based on the CONUS results, however, one would expect greater anomalous synoptic support associated with springtime MCSs in SSA relative to summertime MCSs (Feng et al. 2019; Song et al. 2019). To test the hypothesis that this is also true for SSA, this section presents daily time-lagged composite anomalies before and after the identification of WCC events by TRMM PR in the La Plata basin region (black box in Fig. 1) during SON and DJF. To place the anomalies into context of the climatology, Fig. 2 shows the climatological 250-hPa wind speeds over SSA. Both seasons are characterized by a 250-hPa wind speed maximum over northern Argentina (Fig. 2). During SON, this maximum of nearly 40 m s^{-1} is centered over 30°S across the Andes Mountains and the La Plata basin is located under the jet streak and downwind of a weak upper-level trough (Fig. 2a). In contrast, the DJF wind speed pattern is much weaker at 30°S and the maximum is located farther poleward over the Pacific and Atlantic Oceans (Fig. 2b). These climatological differences in jet stream strength and position likely result in varying large-scale environmental factors such as widespread ascent, which is discussed throughout the study. We also suspect that larger WCCs are associated with more anomalous synoptic patterns; this relationship is explored in sections 3a and 3b by comparing synoptic anomalies of the largest and smallest WCCs.

a. *Synoptic evolution of environments supporting large WCCs*

Large WCCs are defined as those with an areal extent greater than or equal to the 90th percentile of all WCCs

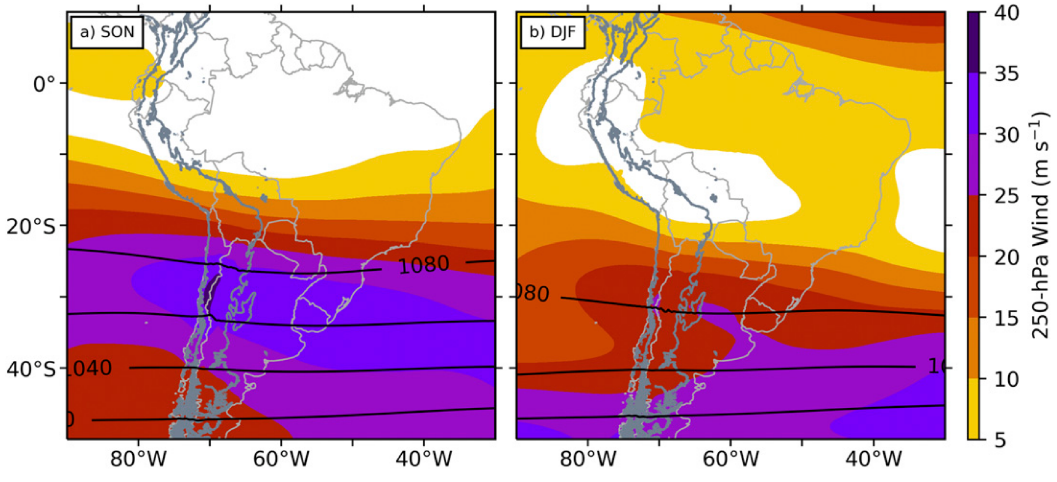

FIG. 2. Climatological 250-hPa wind speed (shaded) and height (black contours every 20 dam) averaged from 1979 to 2018 via ERA5 for (a) SON and (b) DJF. The thick gray contour outlines terrain height of 500 m, highlighting the Andes and SDC of western South America.

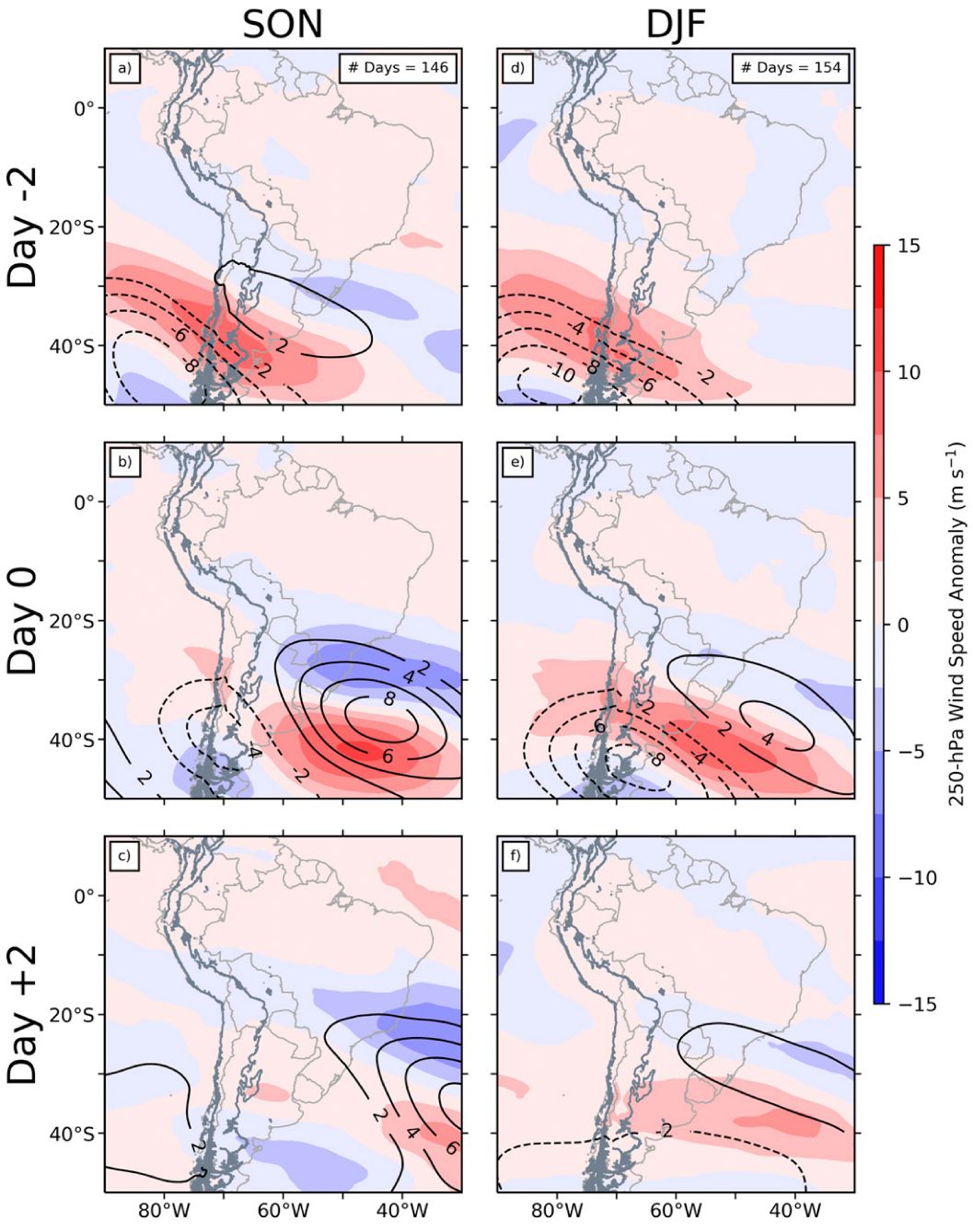

FIG. 3. Time-lagged 250-hPa wind speed (shaded) and height (black contours every 2 dam) composite anomalies for days in which TRMM PR identified a large WCC in the study domain during (a)–(c) SON and (d)–(f) DJF on (a),(d) day −2; (b),(e) day 0; and (c),(f) day +2. The thick gray contour outlines terrain height of 500 m, highlighting the Andes and SDC of western South America. The values in the upper-right corners of (a) and (d) show the number of WCC days that contribute to the composite. These totals are also shown in Table 1.

observed by TRMM PR in the study domain (Fig. 1) during SON (146 unique days) and DJF (154 unique days) from 1998 to 2013 (Table 1). Time-lagged composite anomaly synoptic maps are calculated by subtracting the seasonal climatology (as in Fig. 2) from the large WCC composites and serve as proxies for large-scale patterns such as jet streaks and synoptic troughs/ridges. Additionally, several full (non-anomalous) composite fields are available as supplemental figures as indicated.

Figures 3a–c and 3d–f present 250-hPa wind speed and geopotential height composite anomalies for large WCCs in SON and DJF, respectively. Figure S1 in the online supplemental

material is the same as Fig. 3, but with full field composites. Two days before WCC identification (day −2) in both seasons, a 250-hPa wind speed anomaly of about 10 m s^{-1} is present over the Andes just north of 40°S (Figs. 3a,d). While the spatial extent of this jet anomaly is greater during SON, 250-hPa heights are anomalously lower west of the southern Andes during DJF where an upper-level trough approaches the continent (Figs. 3a,d). On the day of WCC identification (day 0) in both seasons, the positive jet and height anomaly minima/maxima have moved eastward (Figs. 3b,e). SON anomalous wind speeds have increased at the jet maximum from day −2 to 0, but decreased to its north (Fig. 3b). DJF 250-hPa negative height anomalies remain greater in magnitude than SON from day −2 to 0 as this deep trough crosses the Andes farther south than in SON (Fig. 3e). The SON positive wind speed anomaly on day 0 is farther eastward and a jet streak left entrance region is likely over the plains as opposed to over the terrain as in DJF (Fig. 3b, Fig. S1b). Though an upper-level ridge builds downstream over the Atlantic Ocean during both seasons, the corresponding positive height anomalies are about 4 dam greater in SON than in DJF (Figs. 3b,e). The wind speed and height anomalies continue eastward two days following a large WCC event (day +2), though at a slower pace for the less robust DJF anomalies (Figs. 3c,f). Both upper-level trough signals virtually vanish, leaving only a trace of a negative height anomaly in DJF (Fig. 3f). Overall, Fig. 3 suggests that there are similar jet structures between SON and DJF that create favorable regions for large-scale ascent in the La Plata basin; however, ascent in SON is favored over the plains as opposed to near the foothills of the terrain in DJF (Figs. 3b,e, Figs. S1b,e). An upper-level ridge forms downstream likely due to convective processes in SSA as the trough crosses the Andes Mountains (Maddox 1983). These trough–ridge interactions are diagnosed next via 500- and 850-hPa height anomalies.

Figures 4 and 5 show the daily evolution of 500- (black contours) and 850-hPa (shaded) geopotential height anomalies surrounding large WCC events in SON and DJF, respectively. Full field composites are also available as Figs. S2 and S3. Three days prior to large WCC identification in SON, substantial negative geopotential height anomalies at both levels, indicating a deep trough, are located west of Chile centered at approximately 45°S (Fig. 4a). The 500-hPa geopotential height anomaly minimum exceeds −60 m and the 850-hPa exceeds −40 m in magnitude. Geopotential heights are near average over Argentina at this time, with a weak 850-hPa ridge farther downstream over the Atlantic Ocean. The upstream trough intensifies as it starts to impinge upon the Andes two days prior to large WCC events (Fig. 4b), likely an effect of the tall mountain barrier blocking midlevel flow. Simultaneously, a low-level lee trough appears over central Argentina through the process of lee cyclogenesis as a ridge builds downstream over the Atlantic Ocean. As the synoptic trough crosses the terrain and weakens (Figs. 4c,d), consistent with Davis (1997), Schultz and Doswell (2000), and Rasmussen and Houze (2016), the low-level lee trough continues to intensify as a result of adiabatic warming via dry air subsidence from the high terrain, resembling the lee cyclogenesis process that has been observed in this region (Chung 1977; Satyamurty et al. 1990; Gan and Rao 1994; Rasmussen and Houze 2016). By the time the midlevel trough is directly over the Andes near 40°S on day 0 (Fig. 4d), it is weaker and moves more rapidly eastward such that the midlevel trough–ridge pattern becomes only slightly out of phase with the low-level counterpart (Figs. 4e,f).

The DJF 500- and 850-hPa geopotential height anomalies associated with large WCC events (Fig. 5; full field composites in Fig. S3) generally follow a similar temporal trend to those of SON (Fig. 4; full field composites in Fig. S2) with some differences in intensity and location. First, during DJF, the anomalous deep trough impinging upon the Andes from the west is weaker and farther southeastward initially at both levels (Fig. 5a). Its proximity closer to the Andes at day −3 suggests that the movement is slower initially than SON, consistent with the climatologically weaker jet stream in this season (Fig. 2). From day −2 through day −1, the anomalous impinging trough intensifies at midlevels such that 500-hPa geopotential height anomalies exceed −70 m in magnitude (Figs. 5b,c), which is more robust and farther south than SON at this stage (Figs. 4b,c). The trough crosses the Andes near 45°S by day 0, inducing a similar low-level lee trough that is weaker, farther south, and moves eastward more rapidly than that in SON (Figs. 5e,f).

While both SON and DJF feature an anomalously deep trough impinging upon the Andes from the west prior to large WCC identification in the La Plata basin, the anomalous SON 850-hPa lee trough is more robust. This seasonal contrast in low-level lee trough intensity is important because the resulting enhanced north–south pressure gradient force directly relates to SALLJ strength, depth, and thus, moisture transport and precipitation in the region (Marengo et al. 2002, 2004; Salio et al. 2002, 2007; Saulo et al. 2007; Romatschke and Houze 2010; Rasmussen and Houze 2011, 2016; Montini et al. 2019). The lee trough contrast between seasons is likely a result of the poleward shift of the impinging trough from SON to DJF. Because the impinging trough during SON extends deeper vertically such that negative height anomalies cross the Andes farther equatorward (cf. Figs. 4d, 5d) where the Andes are substantially taller (Fig. 1), more midlevel flow is likely blocked by terrain. To conserve potential vorticity, additional stretching of an air column via greater downstream descent from high terrain enhances rotation and lee cyclogenesis, resulting in a stronger low-level lee trough (Kasahara 1966; Smith 1984, 1986; Schultz and Doswell 2000). The key driver of this meridional shift in trough axis with season is radiational surface heating, which is greatest in the subtropics over the summer, pushing the zone of greatest baroclinic instability poleward in DJF. The result is weaker synoptic forcing over Argentina in summer versus spring, although it is well known that SSA features frequent synoptic activity and cold fronts in the summer relative to the CONUS (Garreaud and Wallace 1998). Similarly, Rasmussen and Houze (2016) used terrain modification mesoscale modeling experiments to demonstrate that midlatitude troughs crossing higher Andes terrain lead to stronger synoptic forcing, including a stronger lee trough, SALLJ, and CAPE. The current study builds on Rasmussen and Houze (2016) by showing that the DJF anomalous synoptic forcing of large WCCs is notably greater than the anomalous forcing for all sizes of WCCs (Fig. 4 vs Fig. 3 in Rasmussen and Houze 2016). A

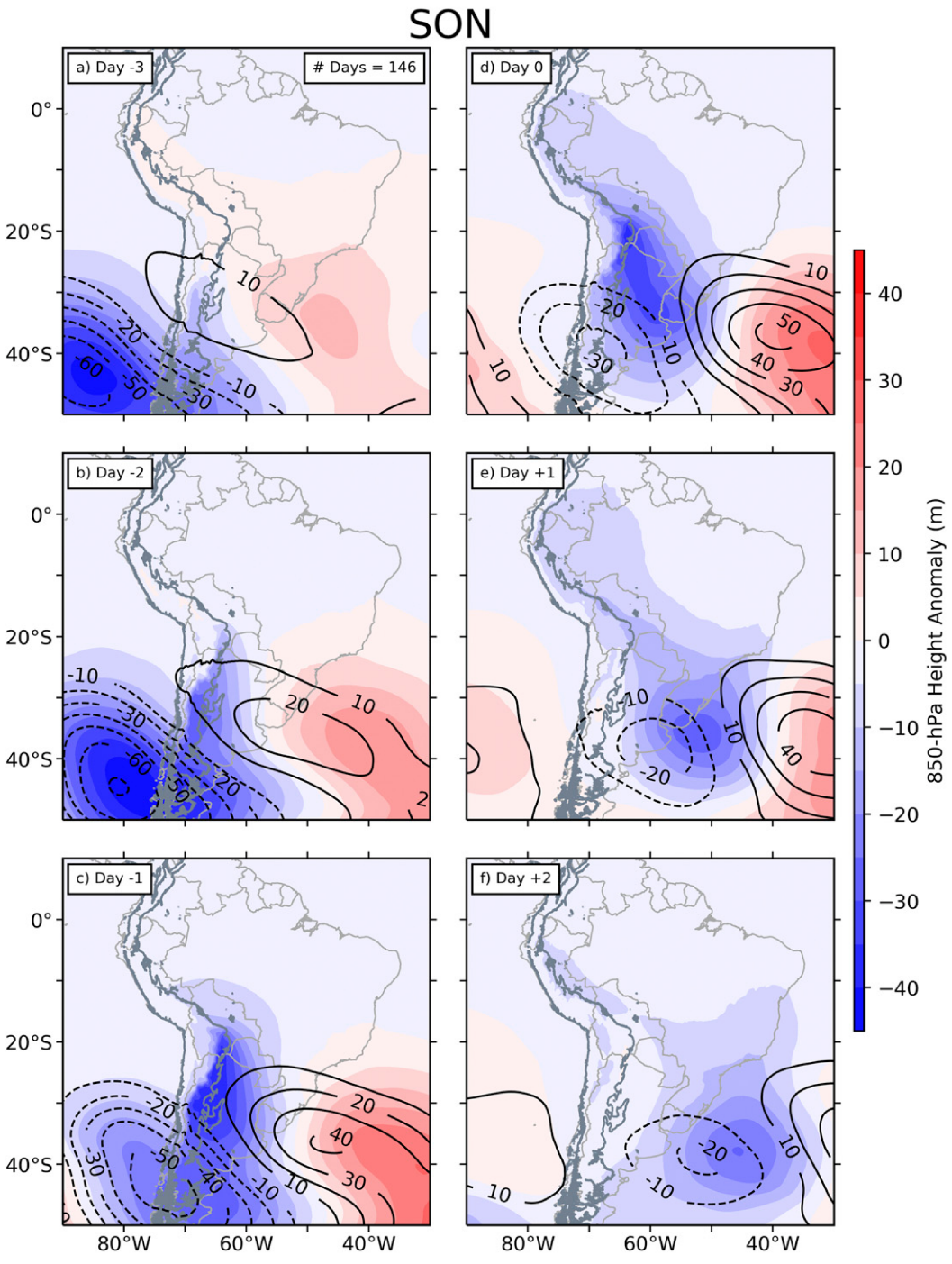

FIG. 4. Time-lagged 850-hPa height (shaded) and 500-hPa height (black contours every 10 m) composite anomalies for days in which TRMM PR identified a large WCC in the study domain during SON on (a) day −3, (b) day −2, (c) day −1, (d) day 0, (e) day +1, and (f) day +2. The thick gray contour outlines terrain height of 500 m, highlighting the Andes and SDC of western South America. The value in the upper-right corner of (a) shows the number of WCC days that contribute to the composite. These totals are also shown in Table 1.

similar conclusion for SON is drawn in section 3b where environments supporting small WCCs are analyzed.

The SALLJ plays a crucial role in transporting moisture from the Amazon basin into SSA, a key ingredient for deep convection initiation east of the Andes (Salio et al. 2007; Insel et al. 2010; Romatschke and Houze 2010; Rasmussen and Houze 2011, 2016; Jones 2019). Though this moisture can reach depths up to 700 hPa, it tends to maximize around 850 hPa

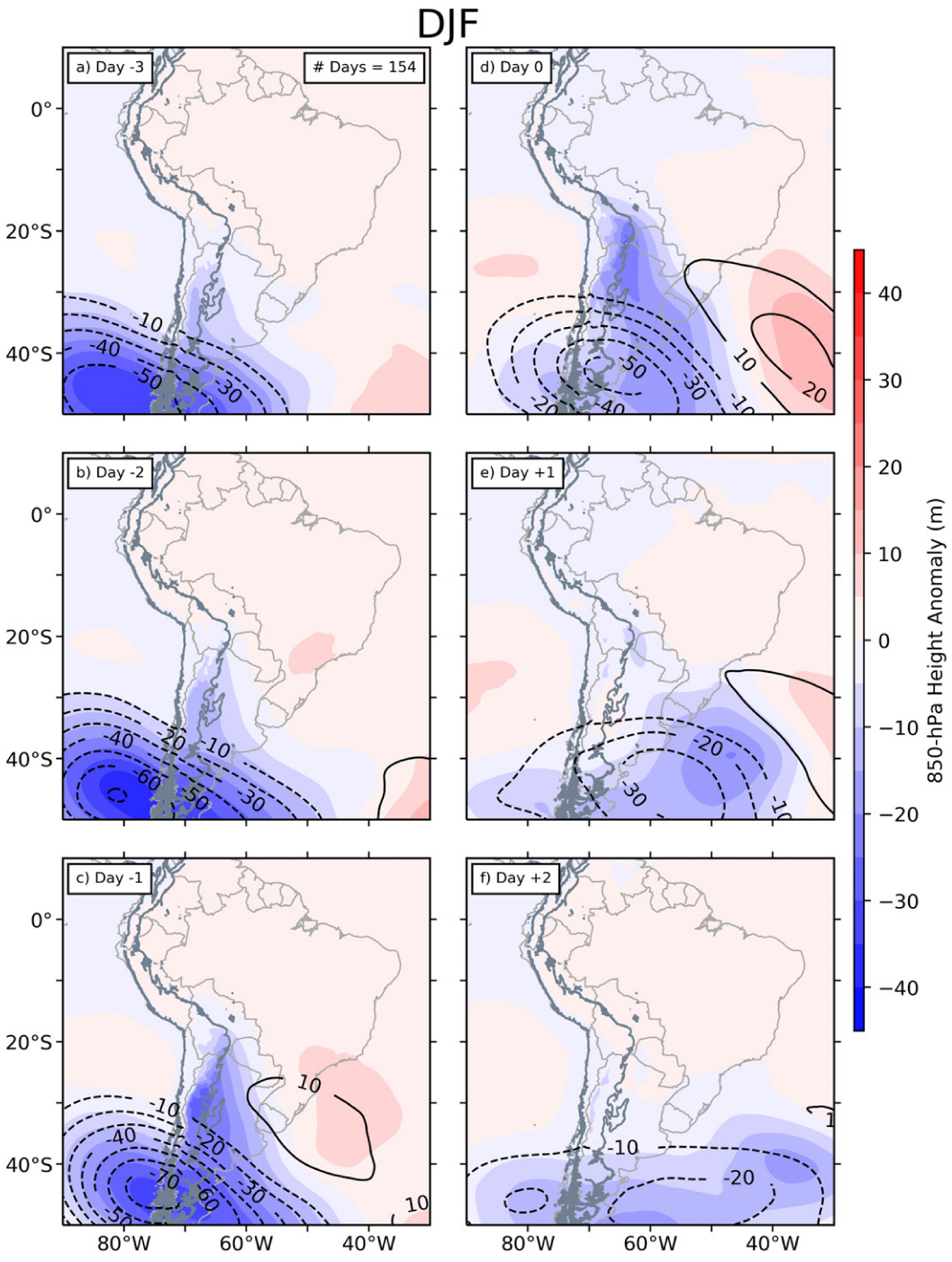

FIG. 5. As in Fig. 4, but for DJF.

(Vera et al. 2006; Oliveira et al. 2018; Piersante et al. 2021). Figures 6 and 7 present the evolution of 850-hPa wind and integrated water vapor transport[1] composite anomalies, respectively, where shading represents the meridional anomaly and arrows show the composite vectors in each figure. Full field composites of 850-hPa wind are also available in Fig. S4. There are widespread northerly 850-hPa winds on day −2 in both SON and DJF (Figs. 6a,d) resulting in northerly moisture flux (Figs. 7a,d). As expected based on the relative magnitudes of the low-level lee troughs between the spring and summer (Figs. 4b and 5b), the actual (Fig. S4) and anomalous (Figs. 6a,d) northerly wind into the La Plata basin

[1] See Copernicus Climate Change Service (2017) for the integrated water vapor transport calculation in ERA5.

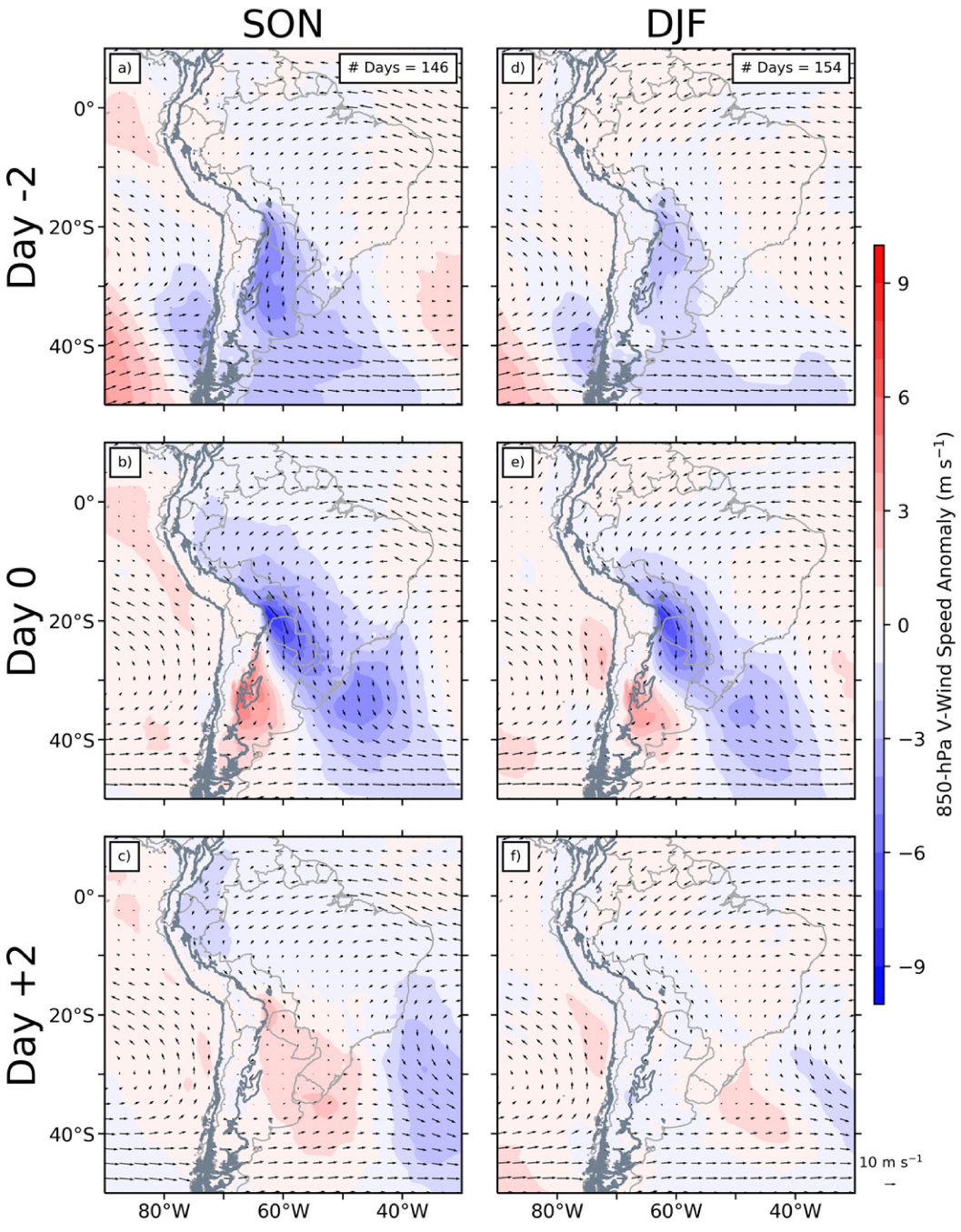

FIG. 6. As in Fig. 3, but for 850-hPa meridional wind speed anomalies (shaded). Arrows represent the composite wind vector, rather than the composite anomaly. The vector scale is placed beneath the color bar.

is greater in SON on day −2. The role the Andes play in channeling moisture is evident as in Insel et al. (2010) and Rasmussen and Houze (2016). While the meridional water vapor flux is similar between seasons (Figs. 7a,d), with a standard anomaly of about 1 sigma near the SDC during both SON and DJF, it exceeds 2 sigma east of the Bolivian Andes as a result of the proximity to the Amazon basin (not shown).

On day 0, anomalous southerly flow at 850 hPa covers central Argentina as the lee cyclone intensifies and moves eastward while the midlevel synoptic trough moves over the Andes (Figs. 4d, 5d, 6b,e; Rasmussen and Houze 2016). As described in Garreaud and Wallace (1998), low-level convergence is likely induced between the northern and southern air masses, causing upward motion to aid upscale growth of SSA MCSs (Rasmussen and Houze 2011). While the deformation zone in

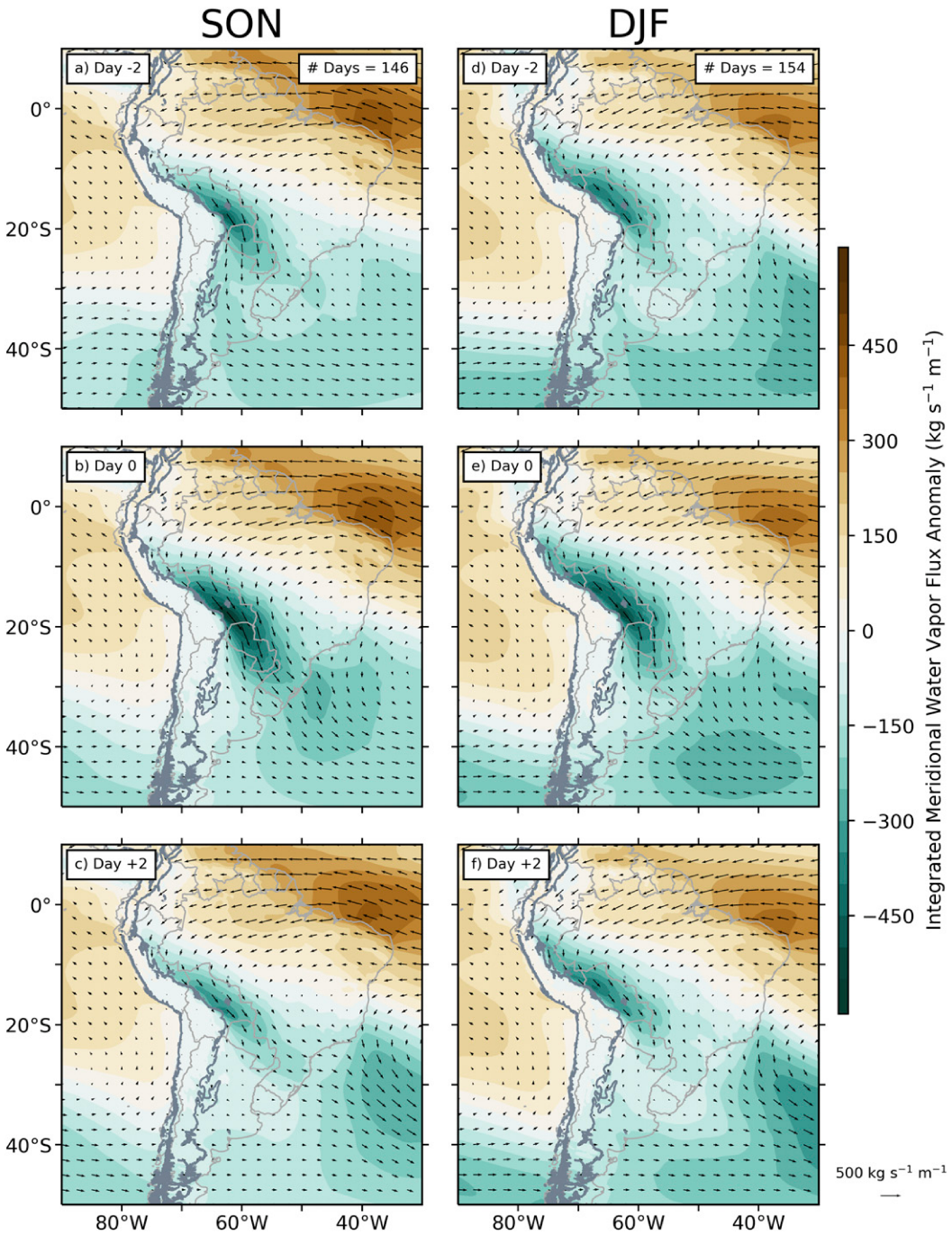

FIG. 7. As in Fig. 3, but for integrated meridional water vapor flux anomaly (shaded). Arrows represent the composite water vapor flux vector, rather than the composite anomaly. The vector scale is placed beneath the color bar.

which low-level convergence likely exists is centered over the northern SDC in DJF (Fig. 6e), it is located farther northeast in SON (Fig. 6b), similar to the meridional placement of the midlevel impinging trough (Figs. 4d and 5d). The implications of such deformation zones on convergence and vertical motion are more carefully assessed in section 4. The full 850-hPa meridional wind fields also suggest that DJF meridional wind gradients and lee cyclones are weaker and located farther poleward (Fig. S4). The bulk of the northerly wind and moisture flux weakens near the SDC as the low-level lee trough passes eastward by day +2, indicating the cessation of synoptic forcing in the region (Figs. 6c,f and 7c,f).

Synoptic troughs induce low-level northerly moisture advection into the La Plata basin prior to and during the presence

of the largest WCCs in SON and DJF (Fig. 7); however, the anomalous flux associated with large WCCs is approximately double that of WCCs of all sizes in DJF (Rasmussen and Houze 2016). Furthermore, while large WCCs in SON are associated with a slightly greater northerly 850-hPa wind speed and moisture flux composite anomalies (Figs. 6 and 7), the actual flux and northerly 850-hPa meridional wind reach farther poleward in DJF (not shown). Despite the weaker and western focus in DJF large-scale forcing, the number of large WCCs in both seasons is almost equal. To investigate how essential synoptic support is for any size of WCC during these seasons, we next look at a subset of WCCs with the smallest areal coverage.

b. *Synoptic evolution of environments supporting small WCCs*

WCCs with an areal extent less than or equal to the 10th percentile of all WCCs identified in SON and DJF by TRMM PR (Table 1) are labeled small WCCs. Small WCC days are as numerous as large WCC days in DJF (147 vs 154 days, respectively; Table 1) while there are fewer small WCC days in SON (112 vs 146 days; Table 1). This section examines the synoptic-scale evolution associated with small WCCs using a subset of the meteorological variables shown previously.

The 250-hPa wind speed and height anomalies for small WCCs in both seasons is presented in Fig. 8 and the full field composites are in Fig. S5. The evolution of 250-hPa SON wind speed and geopotential height anomalies associated with small WCCs is similar to large WCCs; however, the magnitudes are much less (Figs. 8a–c). For example, the positive wind speed anomaly is about 2.5 m s^{-1} weaker, and the height anomalous magnitudes are 2–4 dam weaker before and during the presence of a small WCC relative to a large WCC (cf. Figs. 3a,b and 8a,b). Two days following the identification of a WCC in SON, the synoptic setups for small and large WCCs are almost identical (cf. Figs. 3c and 8c). However, there is a stark difference between small and large DJF WCC environments. While strong anomalous wind speeds and geopotential heights are clear for large DJF WCCs (Figs. 3d–f), anomalous synoptic activity at 250 hPa is almost nonexistent for small WCCs suggesting that an anomalous upper-level jet is not required for the occurrence of small WCCs during DJF (Figs. 8d–f). In other words, anomalous synoptic-scale forcing for ascent appears to be a key factor distinguishing between environments supporting small and large WCCs in the summer. The full field 250-hPa composites show that the jet streak is present during DJF small WCCs, though it is weaker than that of SON (Fig. S5).

Though not shown, the evolution of synoptic waves, northerly moisture flux, and implied low-level convergence is similar, including a low-level lee trough that induces the SALLJ, but weaker in anomalous magnitude for small WCCs compared to large WCCs. Thus, the synoptic composite evolutions presented herein show anomalous large-scale forcing varies with WCC size and season. However, there are likely additional mesoscale phenomena supporting deep convection initiation, back-building, and upscale growth into WCCs within these synoptic environments. To identify additional phenomena such as vertical wind shear at finer spatial and temporal scales, section 4 analyzes a multiday MCS case that featured WCCs during RELAMPAGO where high-resolution mobile soundings and *GOES-16* IR brightness temperature data over SSA were available in addition to ERA5.

4. Case study of long-lived WCC events on 10–13 November 2018

The RELAMPAGO field campaign took place in November-December 2018 with primary objectives to observe and collect data from environments supporting deep convection initiation, severe weather, and upscale growth within the vicinity of the SDC. One case in particular met the criteria of all these objectives and featured numerous supercells and MCSs in north-central Argentina during 10–13 November. While long-lived back-building and upstream propagation processes have been studied in the past (Stensrud 1996; Anabor et al. 2008, 2009; Romatschke and Houze 2010; Rasmussen and Houze 2011, 2016; Mulholland et al. 2018), this section advances prior research by utilizing new high-resolution observations from RELAMPAGO such as soundings and GOES IR brightness temperatures to connect the synoptic through mesoscale processes in upscale growing MCSs in SSA. Preliminary analysis of the ground-based Colorado State University C-band Hydrologic Instrument for Volumetric Observation (CSU-CHIVO) radar (Arias and Chandrasekar 2019) suggests four WCCs were located near Córdoba city over this period using a reduced set of criteria (30 dBZ over 800 km^2), as the radar coverage was relatively small compared to the study domain and likely could not identify a full WCC in one scan. This method does not allow us to precisely fit this case within the climatological WCC size distribution discussed prior, as the TRMM dataset ends before 2018, but the fact that a robust ground-based dataset thoroughly captured multiple WCCs over the course of several days makes this a unique case study, nonetheless.

a. *Synoptic environment evolution*

Similar to the SON climatology at 250 hPa (Fig. 2), a robust upper-level jet streak was present over the Andes and central Argentina when there was widespread deep convection in the study domain on 11–12 November (Fig. 9). This 250-hPa wind speed maximum moved eastward from the west coast of Chile on 10 November (Fig. 9a), but remained relatively stationary over west-central Argentina on 11 and 12 November as it continued to develop a meridional orientation (Figs. 9b,c). Meanwhile, an anomalous trough–ridge pattern similar to that seen in the composite analysis for large SON WCCs (Fig. 4), but much greater in magnitude, slowly moved eastward as the Andes blocked the extremely deep trough impinging from the west (Fig. 10). The movement of this anomalous trough from the Pacific Ocean to South America was slower than the large WCC composite of either season (Figs. 4 and 5) as it took an extra day to cross the Andes (Fig. 10). The anomalous geopotential height minimum crossed the Andes on 13 November at about 32°S, at which point the anomalous trough was substantially weaker (Fig. 10f), but still much deeper than the seasonal composite anomalies for SON and DJF (Figs. 4d and 5d).

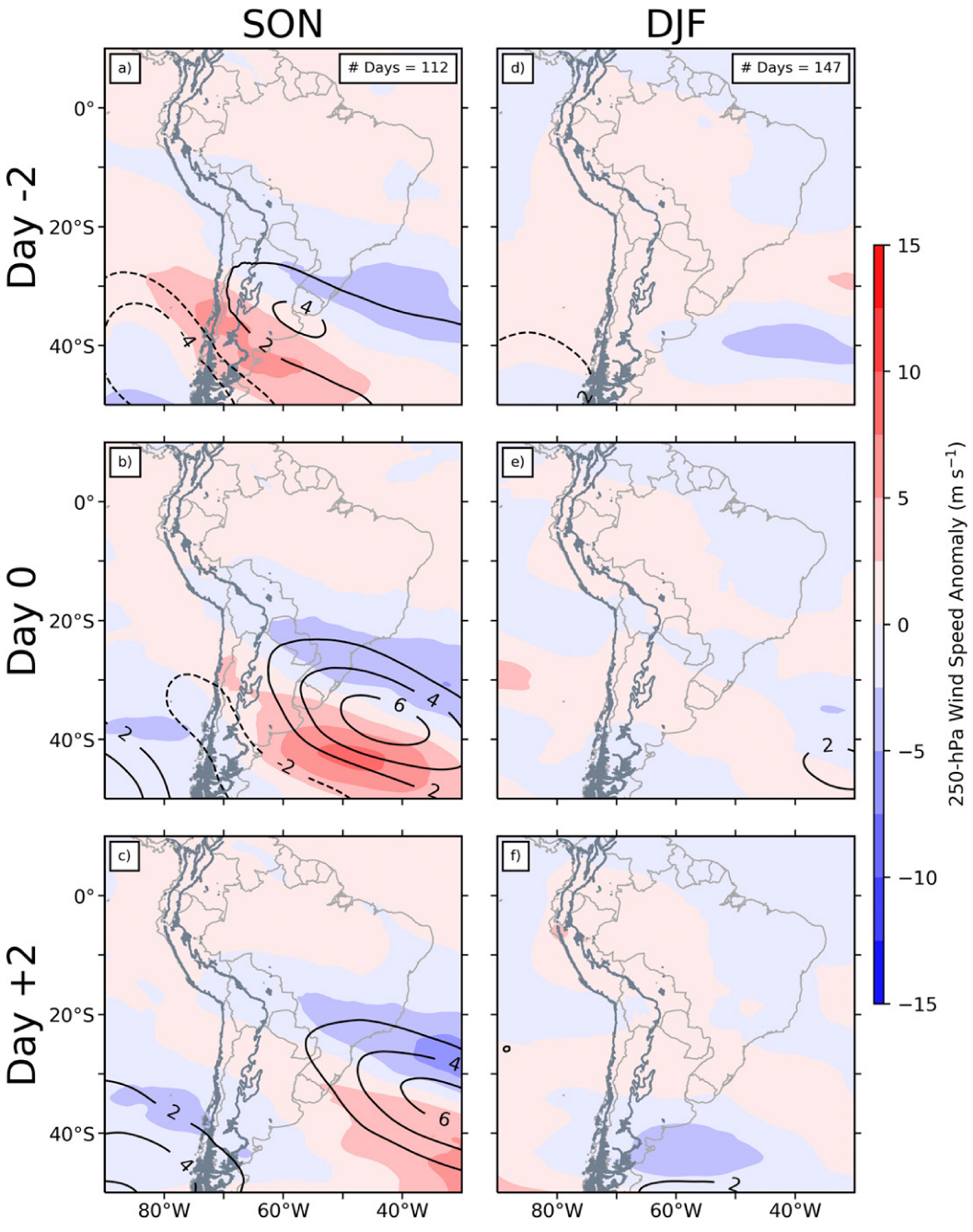

FIG. 8. As in Fig. 3, but for when TRMM PR identified small WCCs in the study domain.

The low-level lee trough was present from 9 to 13 November as a result. In addition to the magnitude of this case, the contrast between the case study and composite anomalies is likely influenced by the varying placement in synoptic waves among cases that contribute to the composite.

A Hovmöller diagram of ERA5 variables is used to link the timing of the slow midlevel trough to the low-level lee trough and widespread deep and organized convection in SSA (Fig. 11). Relatively low IR brightness temperatures averaged over the study domain (224, 236, 248, 256 K; white contours) serve as a proxy for widespread cold cloud tops, which likely result from three upscale growth episodes (U1, U2, U3) following deep convection initiation. These episodes were identified based on substantial expansion of low *GOES-16* brightness temperatures over 6 h (cf. Fig. 13) and are described in more detail in section 4b. During 8–13 November, 500-hPa geopotential heights slowly increased from 5650 m, indicating a weakening midlevel trough approaching the Andes (blue shading becoming lighter on the left) while a ridge built downstream (red shading becoming darker on the right). At 80°W on 11 November,

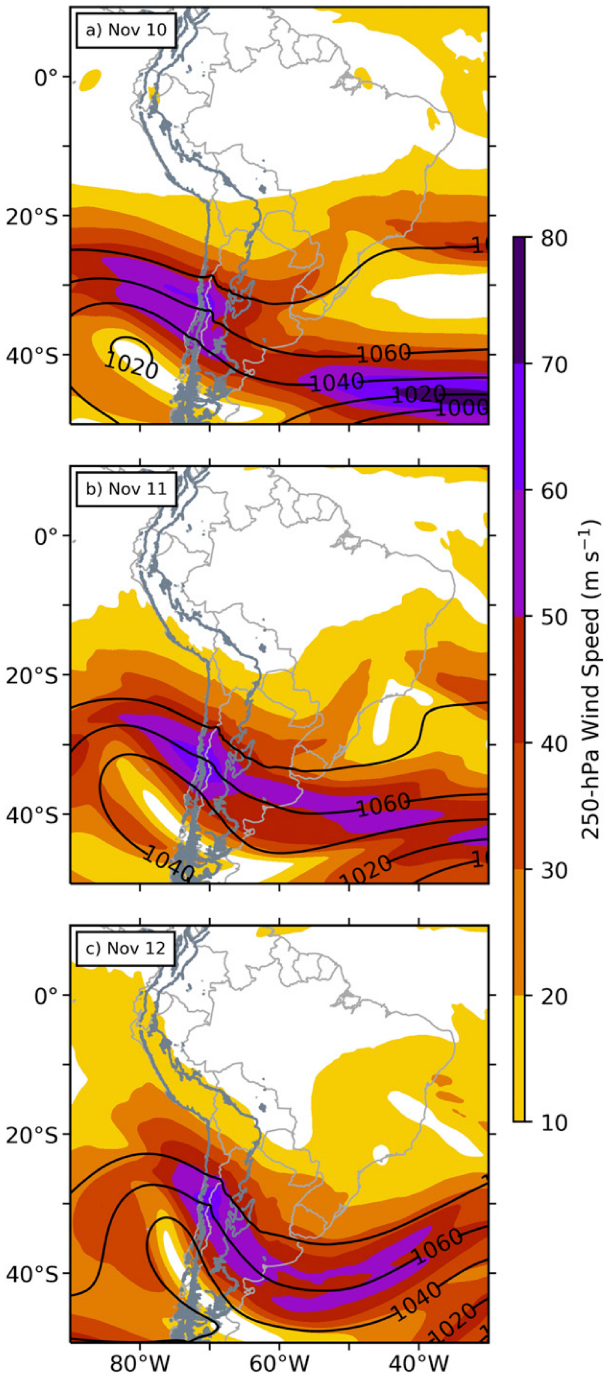

FIG. 9. Daily composites of 250-hPa wind speed (shaded) and height (black contours every 20 dam) for (a) 10, (b) 11, and (c) 12 Nov 2018. The thick gray contour outlines terrain height of 500 m, highlighting the Andes and SDC of western South America.

this trough slowed and 850-hPa geopotential heights and IR temperatures in SSA dropped slightly, representing the development of the low-level lee trough and the first upscale growth episode, U1, east of the Andes (Fig. 11; see also Fig. 13b). This episode featured a supercell thunderstorm within the RELAMPAGO domain; associated mesoscale characteristics such as terrain-enhanced vertical wind shear are more specifically discussed in Trapp et al. (2020), and further details of sounding observations during this episode are discussed by Schumacher et al. (2021). After the midlevel trough became quasi-stationary and started to cross the Andes on 11 November, the low-level lee trough intensified and IR temperatures rapidly decreased, coinciding with the onset of the second upscale growth episode, U2, as deep convection expanded spatially (Fig. 11; see also Fig. 13d). The low-level lee trough persisted through 13 November when the third upscale growth episode, U3, occurred and the midlevel trough weakened while crossing the Andes (Fig. 11; see also Fig. 13f). This suggests that the quasi-stationarity of the trough–ridge system was critical for the multiday, organized deep convection in SSA.

The impact of this synoptic evolution on the low-levels during U2 on 12 November resembles large WCC day 0 synoptic ingredients with much greater intensity (Fig. 12). Specifically, the 850-hPa wind speed (Fig. 12a) and integrated meridional water vapor flux (Fig. 12b) anomalies associated with the SALLJ on this day were approximately 3 times that of the seasonal composite anomalies of large WCCs in SON (Fig. 6b). The moisture flux maximum flowed along the Andes and reached the La Plata basin (Fig. 12b), where it was more than three standard deviations above the mean (not shown). Furthermore, a north–south deformation zone formed between the anomalous southerly flow on the western side of the lee cyclone and the anomalous northerly SALLJ located east of the SDC (Fig. 12a) consistent with the seasonal composites (Fig. 6). A similar pattern developed in the full 850-hPa wind field (not shown). Convergence (Fig. S6a) and ascent at 850-hPa (Fig. S6b) occurred at points along this boundary, which seemed to enable deep convection to initiate as in Garreaud and Wallace (1998). These more intense synoptic anomalies are attributed to the robust, quasi-stationary midlevel trough that impinged upon the Andes for multiple days and locked these conditions in place. This process was suggested by Rasmussen and Houze (2011, 2016), but RELAMPAGO observations enable a more detailed examination into the mesoscale details of upscale growth as described in the following sections.

b. *Mesoscale factors contributing to upscale growth*

Upscale growth episodes U1, U2, and U3 during this multiday event had hints of back-building where deep convection becomes terrain-tied to the SDC (Rasmussen and Houze 2011, 2016) and serial upstream propagation where deep convection grows toward the northwest, against the mean tropospheric flow (Anabor et al. 2008, 2009; Fig. 13). By 1800 UTC (1500 LT) 10 November, a zonal band of cold cloud tops (<215 K) extended eastward from the vicinity of the SDC where supercells with severe hail would soon develop (Fig. 13a). In 6 h, U1 occurred as deep convection back-built westward beyond the terrain of the SDC (Fig. 13b). This event is weakly represented from a Hovmöller perspective using reanalysis IR temperatures over the La Plata basin (Figs. 11 and 14a) likely due to its

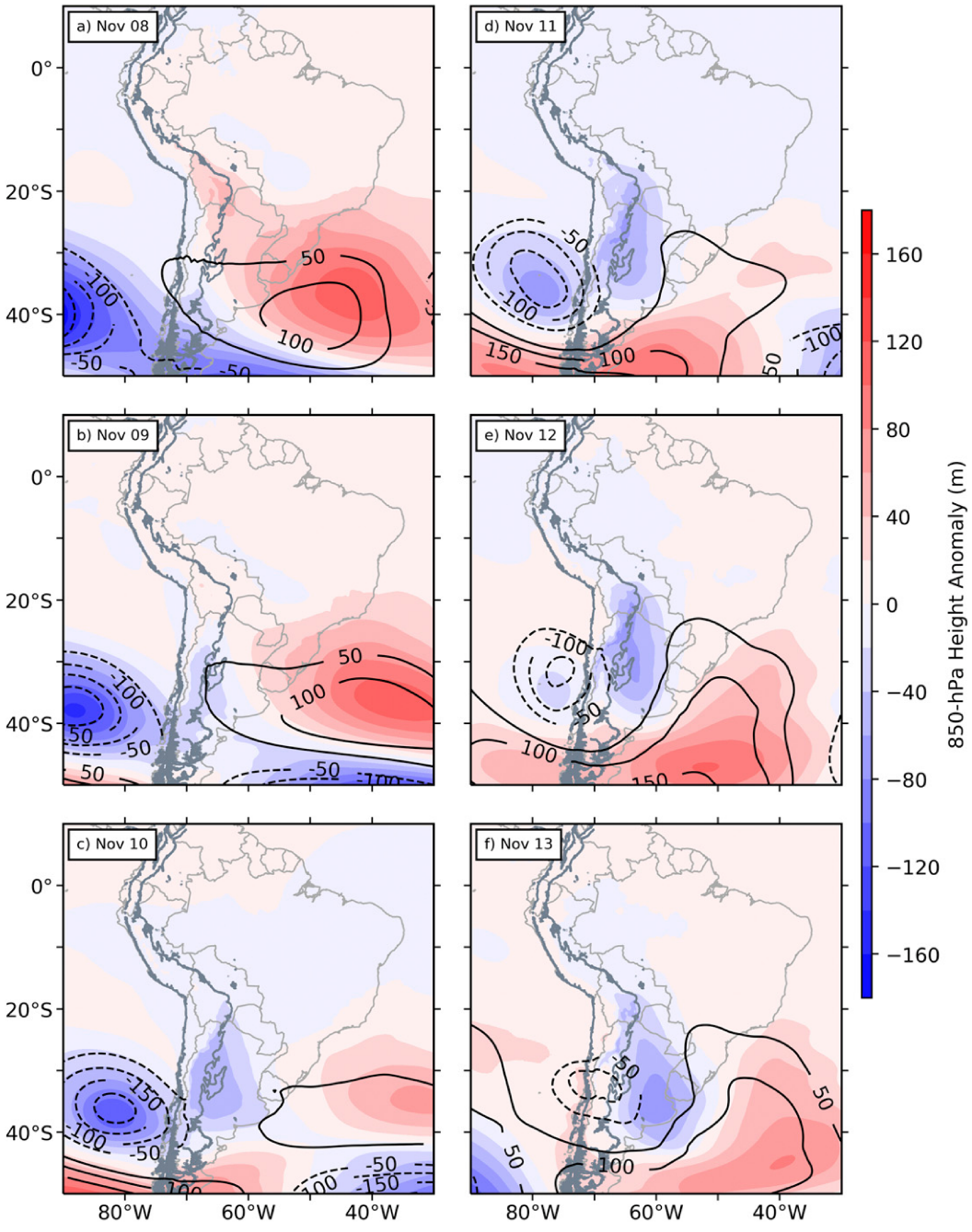

FIG. 10. 850-hPa height (shaded) and 500-hPa height (black contours every 50 m) daily composite anomalies relative to the November 1979–2018 climatology on (a) 8, (b) 9, (c) 10, (d) 11, (e) 12, and (f) 13 Nov 2018. The thick gray contour outlines terrain height of 500 m, highlighting the Andes and SDC of western South America. Note that the 850-hPa height color bar has a broader range than in Figs. 4 and 5.

relatively small spatial extent within the larger Hovmöller domain in which temperatures are averaged. U1 occurred near the SDC in association with moisture flux convergence via the SALLJ (Fig. 14b).

Approximately 24 h later, U2 occurred northeast of Córdoba city along the low-level convergence zone east of the SDC (Fig. 12a) and resulted in multiple MCSs by 0600 UTC (0300 LT; Figs. 13c,d). Discrete, deep convective storms also quickly organized into an MCS in the vicinity of the SDC. Figure 13 does not explicitly showcase the occurrence of terrain-locked back-building along the SDC, though continuous generation of convection in its vicinity demonstrates the need for future investigation. U2 is much more evident than U1 in Fig. 14a because it was more widespread throughout the

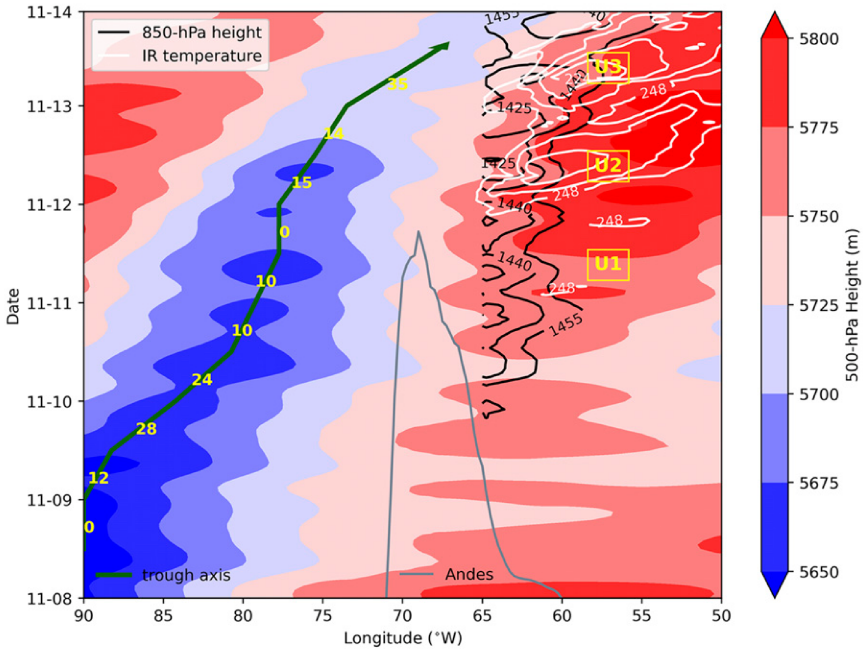

FIG. 11. Hovmöller diagram of ERA5-derived 500-hPa height (shaded) for 50°–90°W averaged between 15° and 50°S during 8–13 Nov 2018. 850-hPa height (1425, 1440, 1455 m; black contours) and IR temperatures (224, 236, 248, 256 K; white contours) averaged between 22° and 36°S for 50°–65°W are also shown to represent the low-level trough and widespread deep convection in the La Plata basin. Fields were smoothed with the SciPy Gaussian filter tool (online at https://docs.scipy.org/doc/scipy/reference/generated/scipy.ndimage.gaussian_filter.html) using sigma = 0.85. The gray contour shows the average relative height of the Andes Mountains between 15° and 50°S with respect to longitude. The green arrow indicates the trough axis, with 12-h averaged eastward ground-relative speeds (km h^{-1}) in yellow, computed assuming that 85 km separates 1° of longitude, which is true at 40°N/S (Williams 2018). Ticks on the *y* axis represent 0000 UTC of that day (local time = UTC − 3 h). Positions of U1, U2, and U3 (yellow boxes) show the time and location of three upscale growth episodes.

La Plata basin. It was also associated with enhanced moisture convergence and the SALLJ (Figs. 14a,b) and a cold front[2] along the SDC (Fig. 13c).

U3 occurred approximately 24 h after U2 as deep convection in northeastern Argentina grew northwestward against the large-scale low-level flow between 1800 UTC (1500 LT) 12 November and 0000 UTC (2100 LT) 13 November to form another mature MCS (Figs. 13e,f). U3 was also potentially influenced by a cold front passing northeastward across northern Argentina (Fig. 13f). U3 featured a stronger (ERA5 IR temperatures < 224 vs < 232 K) and farther eastward minimum in IR temperature than U2 (Fig. 14a), thus terrain likely played less of a role. By this time, the SALLJ at 850 hPa was located farther eastward as well (Fig. 14b).

These deep convective episodes occurred in approximately 24-h intervals with onsets near 0000 UTC (2100 LT) based on Fig. 14a, marking a tie to the diurnal cycle also identified by TRMM in which DCCs typically initiate in the evening and grow upscale into WCCs overnight (Rasmussen and Houze 2011; Rasmussen et al. 2014). Nocturnal pulses of the SALLJ over the course of 3 days were associated with deep convective episodes at these times (Fig. 14b), which was also noted by Vera et al. (2006). The persistence of an enhanced SALLJ seems to be a response to the prolonged low-level lee trough over SSA during the event (Figs. 10 and 11).

Because deep convection in SSA typically initiates in unstable environments following the breaking of a strong capping inversion (Rasmussen and Houze 2011, 2016), identifying how CAPE fluctuates with respect to the diurnal cycle provides more understanding for the recurring upscale growth episodes. To do this, most unstable CAPE (MUCAPE) is calculated from high-resolution stationary and mobile soundings during this case. High-temporal frequency of atmospheric vertical profile observations such as these provided by RELAMPAGO are historically rare to the region and yield a new opportunity for robust analysis of impactful cases like this November event. Generally, MUCAPE at the Córdoba city airport (yellow star in Fig. 12) was large throughout the event, where almost all soundings during 10–13 November exceeded 1000 J kg^{-1} (Fig. 15). Two maxima of 3520 and 3370 J kg^{-1} occurred at 1603 UTC 10 November and 2021 UTC (1303 and 1721 LT) 11 November, respectively, corresponding to a few hours

[2] The surface frontal position is an approximation based on our interpretation of the gridded fields.

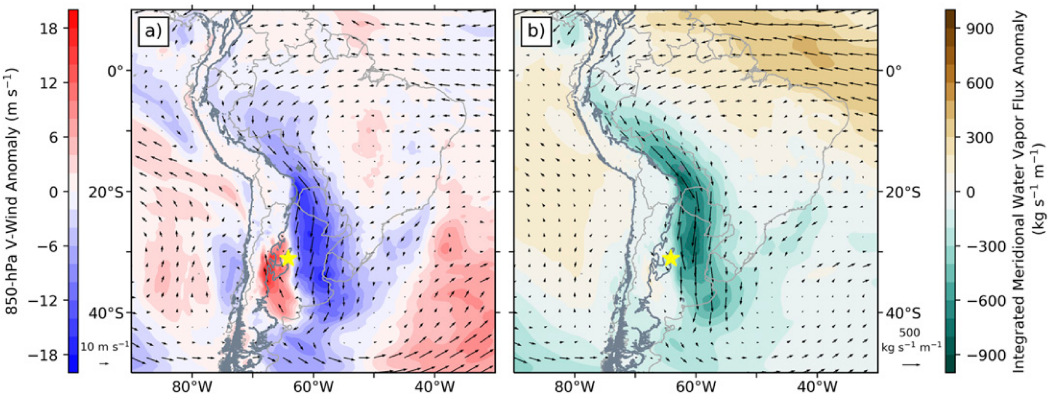

FIG. 12. (a) Daily 850-hPa meridional wind and (b) integrated meridional water vapor flux composite anomalies for 12 Nov 2018 relative to the November 1979–2018 climatology. Arrows represent the composite wind/flux vector rather than the anomaly. The thick gray contour outlines terrain height of 500 m, highlighting the Andes and SDC of western South America. The yellow star shows the location of Córdoba city. Note that the 850-hPa meridional wind and integrated meridional water vapor flux color bars have a broader range than in Figs. 6 and 7, respectively. The vector scales are placed beneath the color bars.

before U1 and U2 (Fig. 15). Mixed layer CAPE followed a similar, yet smaller in magnitude, temporal trend as MUCAPE (not shown). To provide more detail of Córdoba city environments before upscale growth episodes, skew T– log$p$ diagrams corresponding to three sounding launches in Fig. 15 are presented and discussed (Fig. 16).

Before U1 commenced, the 1501 UTC (1201 LT) 10 November sounding had MUCAPE of 2022 J kg^{-1}, with the most unstable parcels in the daytime boundary layer, but also indicated a strong capping inversion (~750 hPa) atop the dry boundary layer. Low-level winds were northerly, but shifted westerly with height suggesting dry air descended from the Andes and likely contributed to this cap (Fig. 16a). Moderate- to strong-shear was present in the lower troposphere where the 0–5-km bulk shear vector magnitude was 20.65 m s^{-1} (Fig. 16a). At 2021 UTC (1721 LT) the next day, low-level winds started to turn southerly while an elevated SALLJ centered near 700 hPa induced northerly moisture advection, marking an increase in lower-troposphere vertical wind shear during U2 that is favorable for mesoscale organization (Fig. 16b; Laing and Fritsch 2000; Coniglio et al. 2006, 2010). The 0–5-km bulk shear increased to 25.68 m s^{-1} as well. As the strong cap was maintained and MUCAPE increased to 3370 J kg^{-1}, there was a transition from surface-based CAPE on 10 November to only elevated CAPE on 11–12 November; this coincided with the apparent passage of a cold front as evidenced by the shift in low-level flow from northerly to southerly (Fig. 13c). By 2000 UTC (1700 LT) 12 November, deep convection matured east and was no longer over Córdoba city (U3; Figs. 13e,f) where southerly near-surface flow and an elevated SALLJ persisted, but MUCAPE dropped to 1094 J kg^{-1} (Fig. 16c). In general, this sounding analysis shows that these MCSs developed in strongly sheared environments following maxima in CAPE and a capping inversion, corroborating the results of Rasmussen and Houze (2011, 2016) using in situ observations.

Hourly soundings from a mobile sounding unit (SCOUT2) near Córdoba city during 2300–0600 UTC (2300–0300 LT) 11–12 November provide a brief window into the evolution of the vertical wind shear and its connection to U2 (Fig. 17; see also Schumacher et al. 2021). An elevated, enhanced northerly SALLJ centered near 700 hPa persisted throughout the time period with wind speeds approaching 20 m s^{-1} while low-level southerly flow below 850 hPa maximized at 0300 UTC (0000 LT) with speeds near 10 m s^{-1} (Fig. 17a). ERA5 generally represents the observed change in meridional wind with height (Fig. 17b) and bulk shear magnitudes of the lowest 100 and 250 hPa of the atmosphere[3] (Fig. 18), both of which provide confidence in the synoptic composite analysis presented in the previous section. However, the ERA5 representation of the nocturnal northerly SALLJ maximum is too weak at this period and is likely due to a well-known issue associated with the low vertical resolution in reanalyses in general (Gensini et al. 2014). The low-level southerly flow was also slightly weaker and more elevated in ERA5 compared to the observations (Figs. 17a,b). Despite this, the reanalysis bulk shear magnitude was greater than the observations early on 12 November (Fig. 18). Overall, there was persistent and robust shear in the lowest 400 hPa through the beginning of U2 with the juxtaposition of the northerly SALLJ and southerly near-surface flow associated with the western edge of the lee trough.

ERA5 is also used to examine the evolution of meridional wind with height with respect to U1, U2, and U3 during 0000 UTC (2100 LT) 10 November to 0000 UTC 14 November over Córdoba city (Fig. 17c). Prior to U1, the SALLJ associated with the western edge of the lee trough extended from the surface to approximately 750 hPa. As the lee trough intensified over central Argentina (Fig. 10d), southerly flow associated with the eastward passage of the lee cyclone began from the surface to 800 hPa during U1 on 11 November (Fig. 17c). As in Figs. 17a and 17b, a similar nocturnal pulse of southerly flow at low levels occurred during U2. Likely a result from the

[3] Bulk shear magnitude was calculated using pressure-level data.

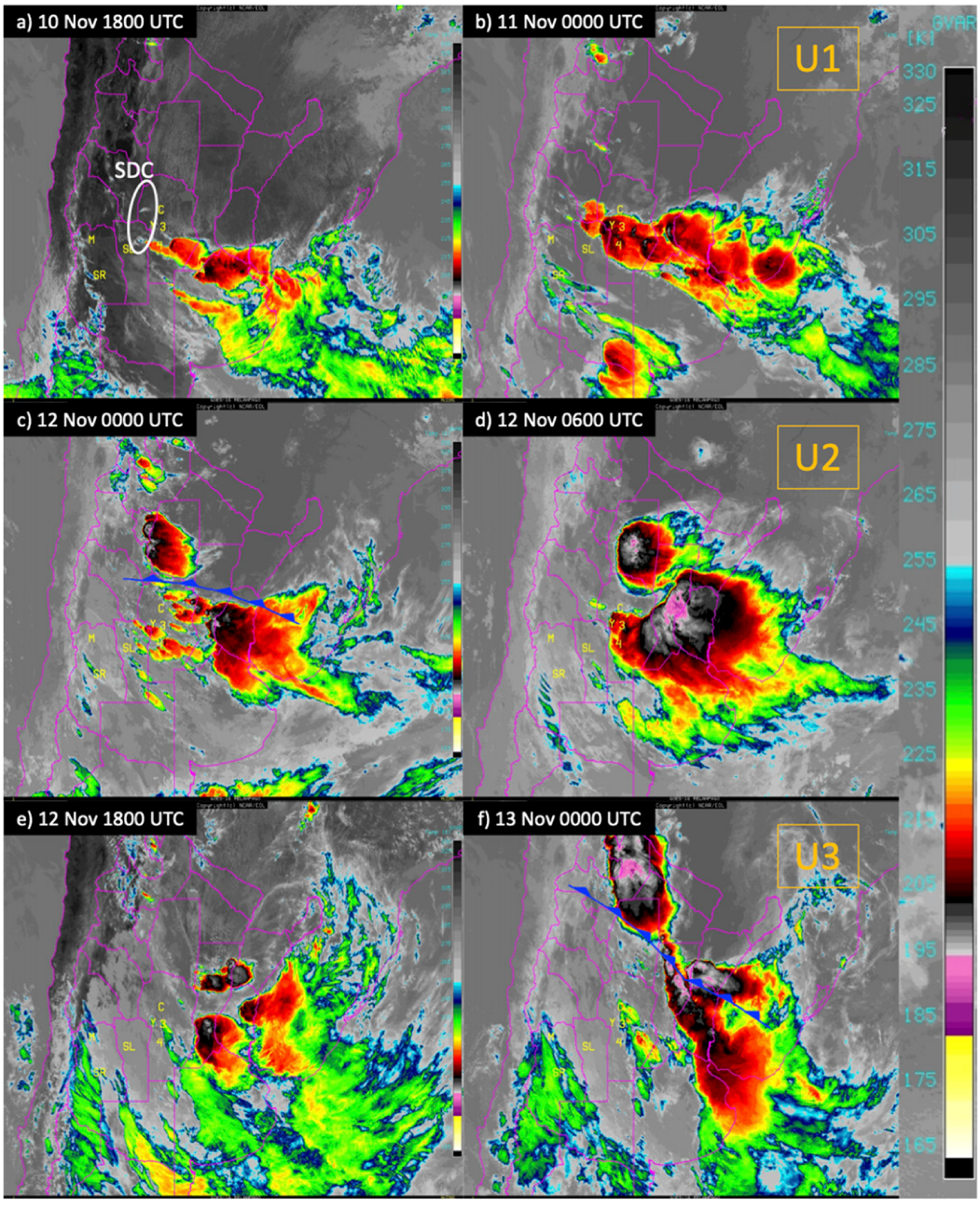

FIG. 13. Three 6-h progressions of upscale growth captured by *GOES-16* IR brightness temperature (shaded) during the November 2018 case over the La Plata basin: (a) 1800 UTC 10 Nov to (b) 0000 UTC 11 Nov; (c) 0000 UTC 12 Nov to (d) 0600 UTC 12 Nov; and (e) 1800 UTC 12 Nov to (f) 0000 UTC 13 Nov. These three periods correspond with upscale growth events U1, U2, and U3. M and C indicate the locations of Mendoza and Córdoba cities; the remaining characters refer to locations used for reference during operations and are irrelevant to this study (e.g., SR, SL, Y, 3, 4). The SDC is roughly outlined in (a). Magenta lines mark provinces of Argentina and coastlines. The approximate cold-frontal location is marked conventionally in (c) and (f), which was estimated from ERA5.

cold-frontal passage, U3 was associated with southerly flow approximately 12 m s^{-1} greater in magnitude at 850 hPa (Fig. 17c) as the SALLJ shifted east of Córdoba city with the low-level lee trough (Fig. 10f). The U3 southerly flow also reached almost 750 hPa where U1 and U2 remained below 800 hPa (Fig. 17c). These results suggest that enhanced, low-level vertical wind shear and convergence caused by the SALLJ and southerly cyclonic flow are associated with the organization of discrete thunderstorms into widespread MCSs. Furthermore, the deepening of southerly flow associated with

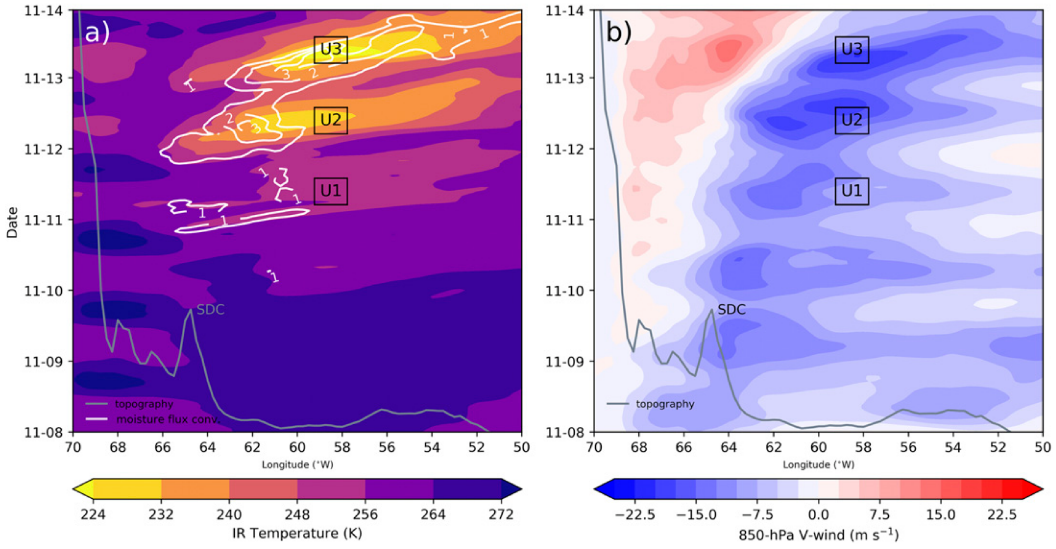

FIG. 14. Hovmöller diagrams of ERA5 (a) IR temperature (K, shaded) and vertically integrated moisture flux convergence (kg^{-2}; white contours) and (b) 850-hPa meridional wind speed (shaded) averaged between 22° and 36°S for 50°–70°W during 8–13 Nov 2018. These fields were smoothed as in Fig. 11. The gray contour shows the relative topography, with the Andes to the west and the SDC at 65°W, calculated by averaging terrain height between 30° and 33°S. Ticks on the *y* axis represent 0000 UTC of that day (local time = UTC − 3 h). Positions of U1, U2, and U3 (black boxes) show the time and location of three upscale growth episodes.

the passage of the low-level lee trough and cold front aid the lifting of unstable air. There are likely additional interactions between cold pools, SDC, and the SALLJ that influence MCS evolution; these should be evaluated by further analysis of radar observations and convection permitting numerical weather prediction models in future studies (e.g., Mulholland et al. 2019).

5. Discussion

The current study expands upon previous work that focused on the generation and maintenance of summertime MCSs in SSA (Romatschke and Houze 2010; Rasmussen and Houze 2011, 2016) by also including an analysis of springtime MCS environments and investigating synoptic conditions conducive for small and large MCSs. MCSs in both seasons are generally characterized by a slow, eastward-moving midlevel trough crossing the Andes Mountains that induces a low-level lee trough and a northerly SALLJ over SSA. We find that synoptic environment anomalies associated with springtime MCSs are greater in magnitude than those associated with summertime MCSs, which is similar to synoptic environments supporting MCSs in the Great Plains of the CONUS (Feng et al. 2019;

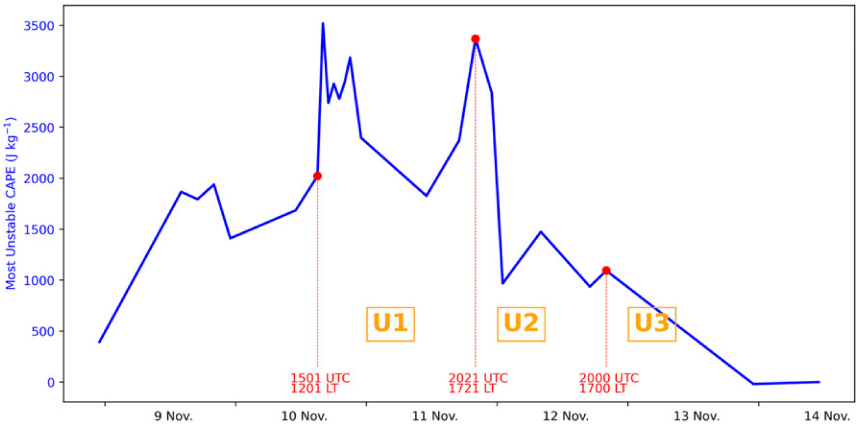

FIG. 15. MUCAPE values from all available Córdoba city airport sounding launches between 2300 UTC (2000 LT) 8 Nov and 1100 UTC (0800 LT) 14 Nov 2018. Positions of U1, U2, and U3 (orange boxes) show the approximate timeframe of three upscale growth episodes. Three soundings further analyzed in Fig. 16 are marked with red points and text corresponding to their launch times.

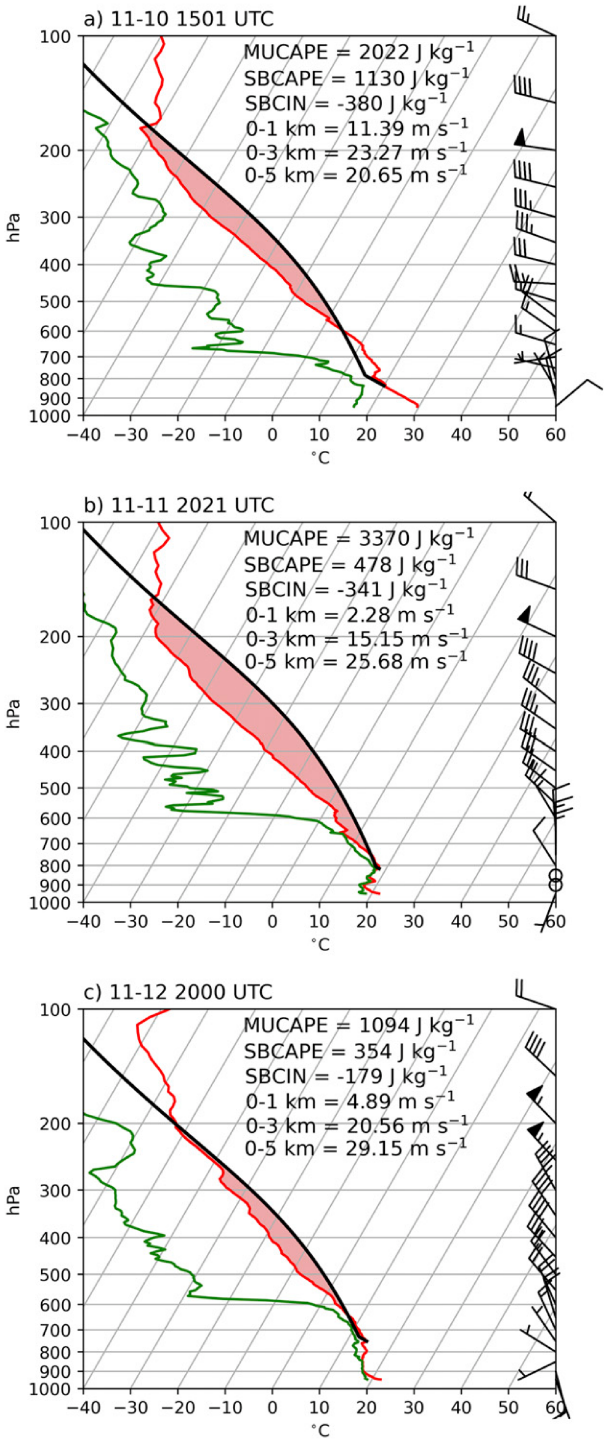

FIG. 16. Skew T–log$p$ diagrams from three soundings launched at Córdoba city Airport: (a) 1501 UTC 10 Nov, (b) 2021 UTC 11 Nov, and (c) 2000 UTC 12 Nov 2018. Pressure (hPa) and °C are the vertical and horizontal coordinates, respectively. Wind barbs on the right side of each skew T–log$p$ diagram indicate direction and speed (short tick = 5 m s^{-1}, long tick = 10 m s^{-1}, and flag = 50 m s^{-1}). Temperature (dewpoint temperature) is plotted in red (green), the most unstable parcel path is in black, and areas of MUCAPE are shaded in red. Values of MUCAPE, surface-based CAPE, and surface-based CIN are shown in the upper-right corner in addition to 0–1-, 0–3-, and 0–5-km bulk wind shear magnitudes.

Song et al. 2019). The current study also addresses the variability of synoptic anomaly magnitudes with respect to MCS size for the first time given that storm size is a simple proxy for severe weather and hydrological impacts. It is found that larger MCSs are associated with greater synoptic-scale anomalies; in particular, small summertime MCSs occurred within relatively weak synoptic environments. Despite weaker anomalous synoptic forcing, summertime MCSs were similar in count to springtime MCSs. Thus, future work must investigate smaller-scale mechanisms responsible for long-lived deep and organized convection in SSA.

Using a new ground-based observation dataset that captured a multiday MCS case during RELAMPAGO in tandem with ERA5, we are able to exemplify the synoptic evolution results previously discussed and identify potential mesoscale factors that could contribute to the longevity of MCSs in SSA where previous studies could not. The longevity of this case seems to be primarily due to a quasi-stationary synoptic pattern that allowed for a persistent baroclinic environment and convergence boundary between the northerly SALLJ and near-surface southerly surge likely associated with a cold front from a lee cyclone. Similar southerly cold surges in the presence of summertime deep convection in SSA have been noted by Garreaud and Wallace (1998). This stable boundary layer flowed beneath the SALLJ, which rapidly enhanced vertical wind shear during the night. The subsequent lifting of unstable air parcels beyond their level of free convection likely helped continue the organization and upscale growth of nocturnal elevated deep convection into the daytime hours.

In several regards, this synoptic setup for long-lived deep convection in SSA mirrors that of the CONUS, in which MCS development is associated with strong vertical wind shear where the southerly flow of the LLJ intercepts westerly flow of a frontal area aloft (Laing and Fritsch 2000; Coniglio et al. 2010; Peters and Schumacher 2015). Additionally, elevated nocturnal deep convection initiation often takes place in large-scale baroclinic regions above a stable boundary layer (Geerts et al. 2017). Much more work has been done in the CONUS to show that when multiday outbreaks of MCSs occur, including those featuring severe weather such as tornadoes, convective feedbacks are responsible for causing quasi-stationary synoptic conditions that allow for persistent favorable environments (Stensrud 1996; Trapp 2014; Chasteen et al. 2019). These long-lived favorable environments often result in precipitation corridors that successive MCSs follow (Tuttle and Davis 2006). Despite similar synoptic setups, MCSs in SSA have longer lifetimes than those in the CONUS (Durkee et al. 2009; Durkee and Mote 2010). We hypothesize that the Andes Mountains, acting as a taller flow barrier than the Rocky Mountains, are responsible for a slower moving midlevel trough and thus longer-lasting favorable conditions for deep

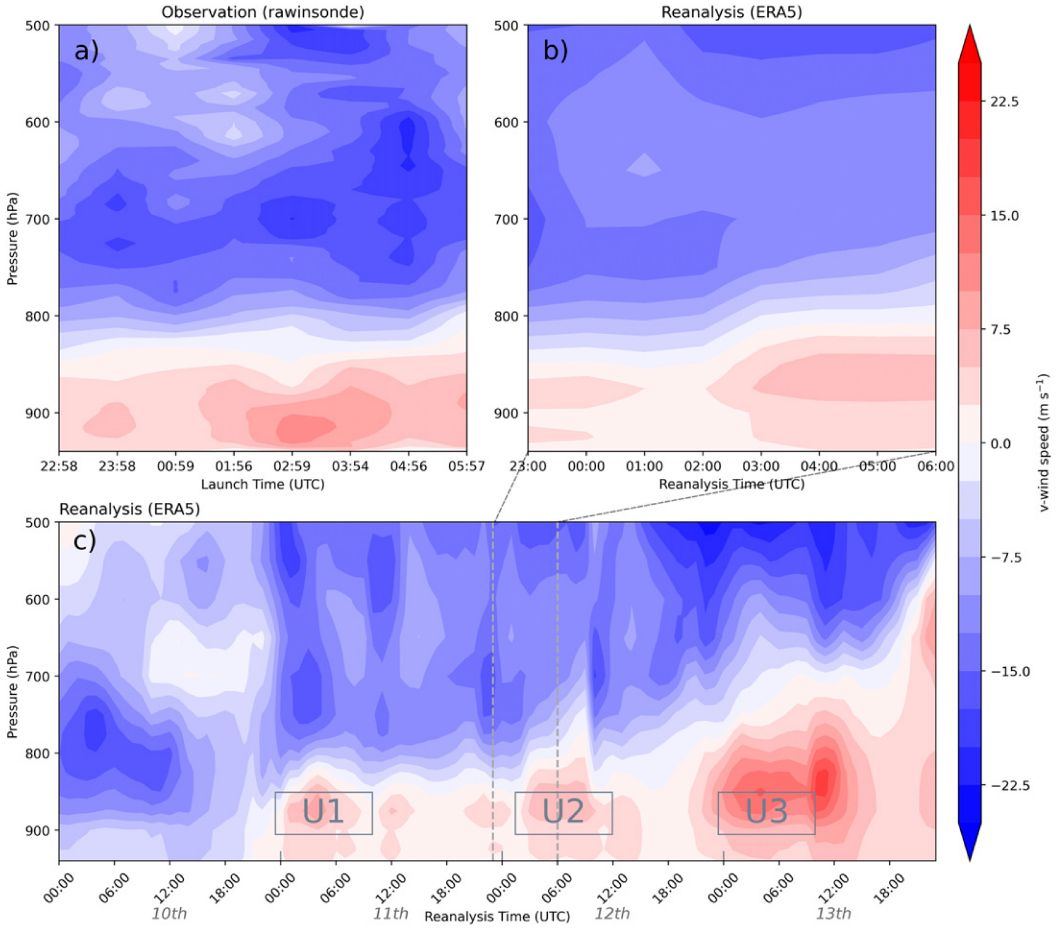

FIG. 17. Meridional wind speed at mobile unit SCOUT2 (31.113°S, 64.138°W) via (a) hourly sounding launches from 2258 UTC 11 Nov to 0537 UTC 12 Nov, (b) hourly ERA5 from 2300 UTC 11 Nov to 0600 UTC 12 Nov, and (c) hourly ERA5 during 10–13 Nov 2018. Note that (b) is a subset of (c), as indicated by dashed black lines; both use reanalysis coordinates of 31.00°S, 64.25°W, which are nearest to the observation location. Reanalysis pressure levels are interpolated to every 5 hPa as in the observational sounding data. U1, U2, and U3 labels (gray boxes) show the time of three upscale growth episodes.

convection east of the mountain range. Within this large-scale environment, various phenomena seem to further prolong convective episodes such as back-building (Rasmussen and Houze 2011, 2016) and upstream propagation (Anabor et al. 2008, 2009). Other multiscale interactions that occur within CONUS MCSs (e.g., frontogenesis, cold pools, topography; Chasteen et al. 2019) likely have an additional influence on SSA MCSs, but continued research with RELAMPAGO data are needed to confirm this parallel.

6. Conclusions

The current study compares the synoptic forcing that supports the largest (≥90th percentile in area) and the smallest (≤10th percentile in area) WCCs in the La Plata basin of Argentina during austral spring (SON) and summer (DJF) using TRMM PR to identify WCCs and ERA5 to create composites of meteorological variables. Generally, the synoptic evolution associated with large WCCs is similar among seasons: an anomalous midlevel trough impinges upon the Andes Mountains from the west multiple days prior to WCC identification in the La Plata basin, leading to an anomalous low-level lee trough over Argentina. The low-level lee trough induces a meridional pressure gradient force associated with the geopotential height difference and enhances the northerly SALLJ that advects low-level moisture from the Amazon basin into Argentina along the Andes before and during the formation of WCCs. Aloft, the left-entrance region of a 250-hPa jet streak over the La Plata basin likely results in synoptic ascent. The impinging trough crossing the Andes induces lee cyclogenesis through potential vorticity conservation and the eastward propagation of the lee cyclone away from the mountains produces a southerly wind shift on the western edge of the lee cyclone and low-level convergence opposing the northerly SALLJ. This evolution and decay of synoptic environments favorable for large WCCs lasts about 6 days as mountain blocking and downstream ridge amplification over the Atlantic Ocean slow synoptic wave propagation.

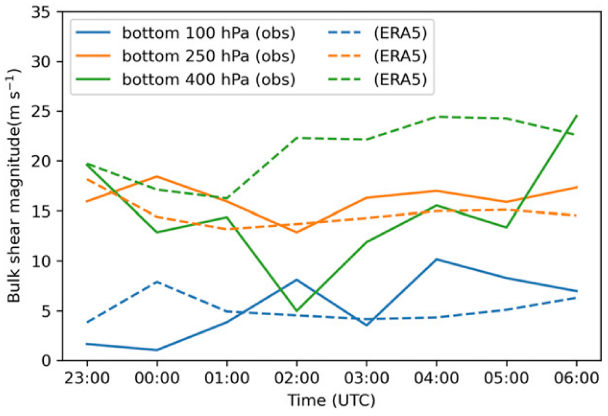

FIG. 18. Hourly layer bulk shear magnitudes from SCOUT2 sounding launches (solid; 31.113°S, 64.138°W; as in Fig. 17a) and corresponding ERA5 (dashed; 31.00°S, 64.25°W; as in Fig. 17b) from 2300 UTC 11 Nov to 0600 UTC 12 Nov calculated from the bottom 100 (blue), 250 (orange), and 400 (green) hPa. Bulk shear magnitude calculated using the MetPy (May et al. 2020) bulk_shear function (online at https://unidata.github.io/MetPy/latest/api/generated/metpy.calc.bulk_shear.html).

The current study is the first to show how the scale of synoptic forcing for large WCCs differs between seasons: the anomalous magnitudes of the impinging 500- and 850-hPa trough heights, 850-hPa lee trough heights, 250-hPa wind speeds, and SALLJ at 850 hPa are all greater in SON. There also appears to be an influence of the impinging trough shifting poleward from SON to DJF; since the height of the Andes decreases poleward, flow blocking, and thus leeside synoptic forcing, decreases into the summer. Furthermore, a reduction in mountain height and flow blocking decreases CAPE and CIN downstream (Rasmussen and Houze 2016). Despite differences in large-scale environments between spring and summer, the number of large WCCs during SON and DJF is almost equal. Anomalous synoptic forcing decreases for small WCCs in both seasons, but especially so for DJF, when small WCCs are more likely and the anomalous jet streak shifts westward over the SDC. This supports the hypothesis of enhanced terrain-induced deep convection initiation and organization in the summer (Romatschke and Houze 2010; Rasmussen and Houze 2011, 2016) and explains the westward shift in WCC frequency and rainfall contribution toward the SDC from SON to DJF (Rasmussen et al. 2016). To solidify the composites presented herein, future work should assess the variability of storm-scale processes that are implied in this study, such as location and intensity of low-level convergence, lee cyclogenesis, vertical motion, and shear.

To exemplify the synoptic anomaly composite results and investigate additional mesoscale processes through ground-based observations, we analyzed a widespread and long-lasting case from the RELAMPAGO field campaign that spawned multiple MCSs with back-building and upstream propagation over the course of 4 days. Its synoptic evolution followed the large WCC composite results, but with much greater anomaly magnitudes and slower synoptic wave translation speeds that enabled a persistent unstable environment over the La Plata basin. Three upscale growth episodes in northern Argentina lasting ~24 h occurred in a row following maxima in CAPE and CIN, exemplifying the conceptual model of Rasmussen and Houze (2016). Their model, however, does not include midlevel vertical wind shear as a potential contributor to the organization of deep convection in the region. In the CONUS, MCS-organizing vertical wind shear often develops at the intersection of a front and LLJ (Laing and Fritsch 2000; Coniglio et al. 2010; Peters and Schumacher 2015); similarly in SSA, this case and the synoptic composites presented herein suggest that enhanced vertical wind shear results from the juxtaposition of the southerly near-surface flow induced by the lee cyclone and the northerly SALLJ. Additionally, the deep southerly near-surface flow, which is likely associated with a cold front, acts to lift air with nonzero CAPE higher in the troposphere, likely resulting in the areal expansion of deep convection and further upscale growth. It is hypothesized that these multiday events occur more routinely in SSA because the Andes lead to more frequent quasi-stationary synoptic conditions. Additional detailed analysis, perhaps using a convection-permitting numerical weather model, is required to adequately differentiate mechanisms between continents, however.

This study brings several new details to light regarding MCS organization and longevity in one of the world's deep convective hotspots by discussing the importance of the midlevel trough position and progression, the relative lack of anomalous synoptic forcing associated with summertime small MCSs, and the unique juxtaposition of southerly near-surface cold surges and the SALLJ. However, future work must continue to use the unique ground-based observation dataset from RELAMPAGO to solidify additional causes behind MCSs in SSA, such as gravity waves, cold pools, and terrain interactions. Further understanding of MCSs that frequently affect this region in the current climate is crucial for determining how their impacts will change in the future. SSA is an example of one of the most convectively active locations on the planet that historically has lacked ground-based observations. Though TRMM has proven useful for similar regions such as central Africa and the Himalayas (Houze et al. 2007; Zuluaga and Houze 2015; Houze et al. 2015), the current study makes it clear that high-resolution in situ measurements reveal phenomena that satellite remote sensing cannot. Thus, the authors hope this work encourages further global collaboration to acquire the needed ground observations for robust investigations of unique and threatening phenomena worldwide in this ever-changing climate.

Acknowledgments. The authors thank Robert A. Houze, Jr., and Stacy Brodzik at the University of Washington for providing quality-controlled TRMM PR data as well as NCAR/UCAR EOL for managing the RELAMPAGO field data from which *GOES-16* imagery and soundings were drawn. Special thanks to Zach Bruick who contributed code to this study and Clayton Sasaki for providing helpful feedback on these results. Thank you to the editor and anonymous reviewers for helping to improve the manuscript. This research was supported by NSF Grants AGS-1661862, AGS-1661657, and AGS-1661768.

Data availability statement. TRMM PR data are stored on a University of Washington server and is available from this website: http://trmm.atmos.washington.edu/. Quality-controlled soundings in South America were accessed through the RELAMPAGO Data Archive (https://data.eol.ucar.edu/master_lists/generated/relampago/) and *GOES-16* imagery through the RELAMPAGO field catalogue (http://catalog.eol.ucar.edu/relampago). ERA5 was accessed through Copernicus (https://cds.climate.copernicus.eu/cdsapp#!/home).

REFERENCES

Anabor, V., D. J. Stensrud, and O. L. L. de Moraes, 2008: Serial upstream-propagating mesoscale convective system events over southeastern South America. *Mon. Wea. Rev.*, **136**, 3087–3105, https://doi.org/10.1175/2007MWR2334.1.

——, ——, and ——, 2009: Simulation of a serial upstream-propagating mesoscale convective system event over southeastern South America using composite initial conditions. *Mon. Wea. Rev.*, **137**, 2144–2163, https://doi.org/10.1175/2008MWR2617.1.

Arias, I., and V. Chandrasekar, 2019: CSU C-Band radar data, version 1.0. UCAR/NCAR–Earth Observing Laboratory, accessed 24 June 2020, https://doi.org/10.26023/DA1G-MCNC-YB0F.

Augustine, J. A., and K. W. Howard, 1988: Mesoscale convective complexes over the United States during 1985. *Mon. Wea. Rev.*, **116**, 685–701, https://doi.org/10.1175/1520-0493(1988)116<0685:MCCOTU>2.0.CO;2.

Bruick, Z. S., K. L. Rasmussen, and D. J. Cecil, 2019: Subtropical South American hailstorm characteristics and environments. *Mon. Wea. Rev.*, **147**, 4289–4304, https://doi.org/10.1175/MWR-D-19-0011.1.

Cecil, D. J., and C. B. Blankenship, 2012: Toward a global climatology of severe hailstorms as estimated by satellite passive microwave imagers. *J. Climate*, **25**, 687–703, https://doi.org/10.1175/JCLI-D-11-00130.1.

Chasteen, M. B., S. E. Koch, and D. B. Parsons, 2019: Multiscale processes enabling the longevity and daytime persistence of a nocturnal mesoscale convective system. *Mon. Wea. Rev.*, **147**, 733–761, https://doi.org/10.1175/MWR-D-18-0233.1.

Chung, Y.-S., 1977: On the orographic influence and lee cyclogenesis in the Andes, the Rockies and the East Asian Mountains. *Arch. Meteor. Geophys. Bioklimatol.*, **26**, 1–12, https://doi.org/10.1007/BF02246530.

Coniglio, M. C., D. J. Stensrud, and L. J. Wicker, 2006: Effects of upper-level shear on the structure and maintenance of strong quasi-linear mesoscale convective systems. *J. Atmos. Sci.*, **63**, 1231–1252, https://doi.org/10.1175/JAS3681.1.

——, J. Y. Hwang, and D. J. Stensrud, 2010: Environmental factors in the upscale growth and longevity of MCSs derived from rapid update cycle analyses. *Mon. Wea. Rev.*, **138**, 3514–3539, https://doi.org/10.1175/2010MWR3233.1.

Copernicus Climate Change Service, 2017: ERA5: Fifth generation of ECMWF atmospheric reanalyses of the global climate. Copernicus Climate Change Service Climate Data Store, accessed 13 December 2019, https://cds.climate.copernicus.eu/cdsapp#!/home.

Davis, C. A., 1997: The modifications of baroclinic waves by the Rocky Mountains. *J. Atmos. Sci.*, **54**, 848–868, https://doi.org/10.1175/1520-0469(1997)054<0848:TMOBWB>2.0.CO;2.

Durkee, J. D., and T. L. Mote, 2010: A climatology of warm-season mesoscale convective complexes in subtropical South America. *Int. J. Climatol.*, **30**, 418–431, https://doi.org/10.1002/joc.1893.

——, ——, and J. M. Shepherd, 2009: The contribution of mesoscale convective complexes to rainfall across subtropical South America. *J. Climate*, **22**, 4590–4605, https://doi.org/10.1175/2009JCLI2858.1.

Feng, Z., R. A. Houze, L. R. Leung, F. Song, J. C. Hardin, J. Wang, W. I. Gustafson, and C. R. Homeyer, 2019: Spatiotemporal characteristics and large-scale environments of mesoscale convective systems east of the Rocky Mountains. *J. Climate*, **32**, 7303–7328, https://doi.org/10.1175/JCLI-D-19-0137.1.

Gan, M. A., and V. B. Rao, 1994: The influence of the Andes Cordillera on transient disturbances. *Mon. Wea. Rev.*, **122**, 1141–1157, https://doi.org/10.1175/1520-0493(1994)122<1141:TIOTAC>2.0.CO;2.

Garreaud, R. D., and J. M. Wallace, 1998: Summertime incursions of midlatitude air into subtropical and tropical South America. *Mon. Wea. Rev.*, **126**, 2713–2733, https://doi.org/10.1175/1520-0493(1998)126<2713:SIOMAI>2.0.CO;2.

Geerts, B., and Coauthors, 2017: The 2015 Plains Elevated Convection At Night Field Project. *Bull. Amer. Meteor. Soc.*, **98**, 767–786, https://doi.org/10.1175/BAMS-D-15-00257.1.

Gensini, V. A., T. L. Mote, and H. E. Brooks, 2014: Severe-thunderstorm reanalysis environments and collocated radiosonde observations. *J. Appl. Meteor. Climatol.*, **53**, 742–751, https://doi.org/10.1175/JAMC-D-13-0263.1.

Houze, R. A., 2004: Mesoscale convective systems. *Rev. Geophys.*, **42**, RG4003, https://doi.org/10.1029/2004RG000150.

——, D. C. Wilton, and B. F. Smull, 2007: Monsoon convection in the Himalayan region as seen by the TRMM precipitation radar. *Quart. J. Roy. Meteor. Soc.*, **133**, 1389–1411, https://doi.org/10.1002/qj.106.

——, K. L. Rasmussen, M. D. Zuluaga, and S. R. Brodzik, 2015: The variable nature of convection in the tropics and subtropics: A legacy of 16 years of the Tropical Rainfall Measuring Mission satellite. *Rev. Geophys.*, **53**, 994–1021, https://doi.org/10.1002/2015RG000488.

Iguchi, T., T. Kozu, R. Meneghini, J. Awaka, and K. Okamoto, 2000: Rain-profiling algorithm for the TRMM precipitation radar. *J. Appl. Meteor.*, **39**, 2038–2052, https://doi.org/10.1175/1520-0450(2001)040<2038:RPAFTT>2.0.CO;2.

——, ——, J. Kwiatkowski, R. Meneghini, J. Awaka, and K. Okamoto, 2009: Uncertainties in the rain profiling algorithm for the TRMM precipitation radar. *J. Meteor. Soc. Japan*, **87A**, 1–30, https://doi.org/10.2151/jmsj.87A.1.

Insel, N., C. J. Poulsen, and T. A. Ehlers, 2010: Influence of the Andes Mountains on South American moisture transport, convection, and precipitation. *Climate Dyn.*, **35**, 1477–1492, https://doi.org/10.1007/s00382-009-0637-1.

Jones, C., 2019: Recent changes in the South America low-level jet. *npj Climate Atmos. Sci.*, **2**, 20, https://doi.org/10.1038/s41612-019-0077-5.

Kalnay, E., and Coauthors, 1996: The NCEP/NCAR 40-Year Reanalysis Project. *Bull. Amer. Meteor. Soc.*, **77**, 437–471, https://doi.org/10.1175/1520-0477(1996)077<0437:TNYRP>2.0.CO;2.

Kasahara, A., 1966: The dynamical influence of orography on the large-scale motion of the atmosphere. *J. Atmos. Sci.*, **23**, 259–271, https://doi.org/10.1175/1520-0469(1966)023<0259:TDIOOO>2.0.CO;2.

Kummerow, C., W. Barnes, T. Kozu, J. Shiue, and J. Simpson, 1998: The Tropical Rainfall Measuring Mission (TRMM) sensor package. *J. Atmos. Oceanic Technol.*, **15**, 809–817, https://doi.org/10.1175/1520-0426(1998)015<0809:TTRMMT>2.0.CO;2.

Laing, A. G., and M. J. Fritsch, 2000: The large-scale environments of the global populations of mesoscale convective systems.

Mon. Wea. Rev., **128**, 2756–2776, https://doi.org/10.1175/1520-0493(2000)128<2756:TLSEOT>2.0.CO;2.

Maddox, R. A., 1983: Large-scale meteorological conditions associated with midlatitude, mesoscale convective complexes. *Mon. Wea. Rev.*, **111**, 1475–1493, https://doi.org/10.1175/1520-0493(1983)111<1475:LSMCAW>2.0.CO;2.

Marengo, J. A., M. W. Douglas, and P. L. Silva Dias, 2002: The South American low level jet east of the Andes during the 1999 LBATRMM and LBA-WET AMC campaign. *J. Geophys. Res.*, **107**, 8079, https://doi.org/10.1029/2001JD001188.

——, W. R. Soares, A. C. Saulo, and M. Nicolini, 2004: Climatology of the low-level jet east of the Andes as derived from the NCEP–NCAR reanalyses: Characteristics and temporal variability. *J. Climate*, **17**, 2261–2280, https://doi.org/10.1175/1520-0442(2004)017<2261:COTLJE>2.0.CO;2.

Matsudo, C. M., and P. V. Salio, 2011: Severe weather reports and proximity to deep convection over Northern Argentina. *Atmos. Res.*, **100**, 523–537, https://doi.org/10.1016/j.atmosres.2010.11.004.

May, R., S. Arms, P. Marsh, E. Bruning, J. R. Leeman, K. Goebbert, J. E. Thielen, and Z. Bruick, 2020: MetPy: A Python package for meteorological data. UCAR/NCAR–Unidata, accessed 1 November 2019, https://doi.org/10.5065/D6WW7G29.

Montini, T. L., C. Jones, and L. M. V. Carvalho, 2019: The South American Low-Level Jet: A new climatology, variability, and changes. *J. Geophys. Res. Atmos.*, **124**, 1200–1218, https://doi.org/10.1029/2018JD029634.

Mulholland, J. P., S. W. Nesbitt, R. J. Trapp, K. L. Rasmussen, and P. V. Salio, 2018: Convective storm life cycle and environments near the Sierras de Córdoba, Argentina. *Mon. Wea. Rev.*, **146**, 2541–2557, https://doi.org/10.1175/MWR-D-18-0081.1.

——, ——, and ——, 2019: A case study of terrain influences on upscale convective growth of a supercell. *Mon. Wea. Rev.*, **147**, 4305–4324, https://doi.org/10.1175/MWR-D-19-0099.1.

Nesbitt, S. W., R. Cifelli, and S. A. Rutledge, 2006: Storm morphology and rainfall characteristics of TRMM precipitation features. *Mon. Wea. Rev.*, **134**, 2702–2721, https://doi.org/10.1175/MWR3200.1.

——, and Coauthors, 2021: A storm safari in Argentina: Proyecto RELAMPAGO. *Bull. Amer. Meteor. Soc.*, https://doi.org/10.1175/BAMS-D-20-0029.1, in press.

Oliveira, M. I., E. L. Nascimento, and C. Kannenberg, 2018: A new look at the identification of low-level jets in South America. *Mon. Wea. Rev.*, **146**, 2315–2334, https://doi.org/10.1175/MWR-D-17-0237.1.

Peters, J. M., and R. S. Schumacher, 2015: Mechanisms for organization and echo training in a flash-flood-producing mesoscale convective system. *Mon. Wea. Rev.*, **143**, 1058–1085, https://doi.org/10.1175/MWR-D-14-00070.1.

Piersante, J. O., R. S. Schumacher, and K. L. Rasmussen, 2021: Comparison of biases in warm-season WRF forecasts in North and South America. *Wea. Forecasting*, **36**, 979–1001, https://doi.org/10.1175/WAF-D-20-0062.1.

Rasmussen, K. L., and R. A. Houze, 2011: Orogenic convection in subtropical South America as seen by the TRMM satellite. *Mon. Wea. Rev.*, **139**, 2399–2420, https://doi.org/10.1175/MWR-D-10-05006.1.

——, and ——, 2016: Convective initiation near the Andes in subtropical South America. *Mon. Wea. Rev.*, **144**, 2351–2374, https://doi.org/10.1175/MWR-D-15-0058.1.

——, M. D. Zuluaga, and R. A. Houze, 2014: Severe convection and lightning in subtropical South America. *Geophys. Res. Lett.*, **41**, 7359–7366, https://doi.org/10.1002/2014GL061767.

——, M. M. Chaplin, M. D. Zuluaga, and R. A. Houze, 2016: Contribution of extreme convective storms to rainfall in South America. *J. Hydrometeor.*, **17**, 353–367, https://doi.org/10.1175/JHM-D-15-0067.1.

Romatschke, U., and R. A. Houze, 2010: Extreme summer convection in South America. *J. Climate*, **23**, 3761–3791, https://doi.org/10.1175/2010JCLI3465.1.

Salio, P., M. Nicolini, and A. C. Saulo, 2002: Chaco low level jet events characterization during the austral summer season. *J. Geophys. Res.*, **107**, 4816, https://doi.org/10.1029/2001JD001315.

——, ——, and E. J. Zipser, 2007: Mesoscale convective systems over southeastern South America and their relationship with the South American low-level jet. *Mon. Wea. Rev.*, **135**, 1290–1309, https://doi.org/10.1175/MWR3305.1.

Satyamurty, P., C. C. Ferreira, and M. A. Gan, 1990: Cyclonic vortices over South America. *Tellus*, **42A**, 194–201, https://doi.org/10.3402/tellusa.v42i1.11870.

Saulo, C., J. Ruiz, and Y. G. Skabar, 2007: Synergism between the low-level jet and organized convection at its exit region. *Mon. Wea. Rev.*, **135**, 1310–1326, https://doi.org/10.1175/MWR3317.1.

Schultz, D. M., and C. A. Doswell III, 2000: Analyzing and forecasting Rocky Mountain lee cyclogenesis often associated with strong winds. *Wea. Forecasting*, **15**, 152–173, https://doi.org/10.1175/1520-0434(2000)015<0152:AAFRML>2.0.CO;2.

Schumacher, R. S., and Coauthors, 2021: Convective-storm environments in subtropical South America from high-frequency soundings during RELAMPAGO-CACTI. *Mon. Wea. Rev.*, **149**, 1439–1458, https://doi.org/10.1175/MWR-D-20-0293.1.

Smith, R. B., 1984: A theory of lee cyclogenesis. *J. Atmos. Sci.*, **41**, 1159–1168, https://doi.org/10.1175/1520-0469(1984)041<1159:ATOLC>2.0.CO;2.

——, 1986: Further development of a theory of lee cyclogenesis. *J. Atmos. Sci.*, **43**, 1582–1602, https://doi.org/10.1175/1520-0469(1986)043<1582:FDOATO>2.0.CO;2.

Song, F., Z. Feng, L. R. Leung, R. A. Houze Jr., J. Wang, J. Hardin, and C. R. Homeyer, 2019: Contrasting spring and summer large-scale environments associated with mesoscale convective systems over the U.S. Great Plains. *J. Climate*, **32**, 6749–6767, https://doi.org/10.1175/JCLI-D-18-0839.1.

Stensrud, D. J., 1996: Effects of persistent, midlatitude mesoscale regions of convection on the large-scale environment during the warm season. *J. Atmos. Sci.*, **53**, 3503–3527, https://doi.org/10.1175/1520-0469(1996)053<3503:EOPMMR>2.0.CO;2.

——, and J. M. Fritsch, 1993: Mesoscale convective systems in weakly forced large-scale environments. Part I: Observations. *Mon. Wea. Rev.*, **121**, 3326–3344, https://doi.org/10.1175/1520-0493(1993)121<3326:MCSIWF>2.0.CO;2.

Trapp, R. J., 2014: On the significance of multiple consecutive days of tornado activity. *Mon. Wea. Rev.*, **142**, 1452–1459, https://doi.org/10.1175/MWR-D-13-00347.1.

——, and Coauthors, 2020: Multiple-platform and multiple-Doppler radar observations of a supercell thunderstorm in South America during RELAMPAGO. *Mon. Wea. Rev.*, **148**, 3225–3241, https://doi.org/10.1175/MWR-D-20-0125.1.

Trier, S. B., J. H. Marsham, C. A. Davis, and D. A. Ahijevych, 2011: Numerical simulations of the postsunrise reorganization of a nocturnal mesoscale convective system during 13 June IHOP_2002. *J. Atmos. Sci.*, **68**, 2988–3011, https://doi.org/10.1175/JAS-D-11-0112.1.

Tuttle, J. D., and C. A. Davis, 2006: Corridors of warm season precipitation in the central United States. *Mon. Wea. Rev.*, **134**, 2297–2317, https://doi.org/10.1175/MWR3188.1.

Velasco, I., and J. M. Fritsch, 1987: Mesoscale convective complexes in the Americas. *J. Geophys. Res.*, **92**, 9591, https://doi.org/10.1029/JD092iD08p09591.

Vera, C., and Coauthors, 2006: The South American Low-Level Jet Experiment. *Bull. Amer. Meteor. Soc.*, **87**, 63–78, https://doi.org/10.1175/BAMS-87-1-63.

Williams, E., 2018: Latitude/longitude distance calculator. National Hurricane Center, accessed 20 March 2020, https://www.nhc.noaa.gov/gccalc.shtml.

Yang, Q., R. A. Houze, L. R. Leung, and Z. Feng, 2017: Environments of long-lived mesoscale convective systems over the central United States in convection permitting climate simulations. *J. Geophys. Res. Atmos.*, **122**, 13 288–13 307, https://doi.org/10.1002/2017JD027033.

Zipser, E. J., D. J. Cecil, C. Liu, S. W. Nesbitt, and D. P. Yorty, 2006: Where are the most intense thunderstorms on Earth? *Bull. Amer. Meteor. Soc.*, **87**, 1057–1072, https://doi.org/10.1175/BAMS-87-8-1057.

Zuluaga, M. D., and R. A. Houze, 2013: Evolution of the population of precipitating convective systems over the equatorial Indian Ocean in active phases of the Madden–Julian Oscillation. *J. Atmos. Sci.*, **70**, 2713–2725, https://doi.org/10.1175/JAS-D-12-0311.1.

——, and ——, 2015: Extreme convection of the near-equatorial Americas, Africa, and adjoining oceans as seen by TRMM. *Mon. Wea. Rev.*, **143**, 298–316, https://doi.org/10.1175/MWR-D-14-00109.1.